Doctoral School of Geosciences

Quantifying variability of physical /petrophysical properties of Boda Claystone Formation (BCF) using X-ray computed-tomography scan images (CT)

Ph.D. Thesis

Author
Saja Mohammad Ahmed Abutaha

Supervisor
Dr. Sándor Gulyás

Associate professor, Vice head of the department
The University of Szeged, Department of Geology and Paleontology

Consultant
Dr. János Geiger

Associate professor, scientific advisor of GEOCHEM Ltd,
The University of Szeged, Dept. of Geology and Paleontology

Department of Geology and Paleontology
Faculty of Science and Informatics
University of Szeged
2022
Szeged

Table of Contents

1. Chapter I: Introduction 6
1.1. Boda Claystone Formation; General view 6
1.1.1. Geological setting: location, lithology, and mineralogy 6
1.1.2. Depositional environment 8
1.1.3. The importance of Boda Claystone Formation 9
1.1.4. CT principle 10
1.1.5. Applied CT scans 12
1.2. Aims and general workflow 13
2. Chapter II: Evaluation of 3D small-scale lithological heterogeneities and pore distribution of the Boda Claystone Formation using X-ray Computed Tomography images (CT) 17
2.1. Introduction 17
2.2. Analyses workflow 19
2.3. Results 22
2.3.1. CT characters of rock-forming components in the studied core. 22
2.3.2. 3D Spatial patterns within the core 23
2.4. Discussion 32
2.5. Summary 36
3. Chapter III: Assessing the representative elementary volume of rock types by X-ray computed tomography (CT) – a simple approach to demonstrate the heterogeneity of the Boda Claystone Formation in Hungary. 39
3.1. Introduction 39
3.2. Methodology 40
3.2.1. Quantitative analysis of CT volume 40
3.2.2. REV calculations 41
3.3. Results 45
3.3.1. Quantitative analyses of rock types 45
3.3.2. REV calculations of CT density 48
3.4. Discussion 48
3.5. Conclusions 53
4. Chapter IV: Calculating the representative elementary volume of porosity using X-ray computed tomography: Boda Claystone Formation core sample/Hungary. 56
4.1. Introduction 56

4.2. Methods 57
4.3. Results and interpretations 59
4.3.1. Actual and simulated REV values 59
4.3.2. Quantitative analysis of porosity in 4L-1 and 4L-2 CT volumes 60
4.3.3. High porosity REV interpretation / why ought the core sample's middle part not stand for the inceptive volume of the REV calculations? 68
4.4. Summary and conclusion 68
5. Chapter V: Thesis Summary 70
6. Acknowledgment 73
7. References 74

List of Figures

Figure I.1: Distribution of Boda Claystone Formation sequences in the Mecsek Hills area (after Haas & Péró, 2004); B – The studied core site, Ibafa 4 (Ib-4),.....5

Figure I. 2: The core and the intervals studied by CT. Abbreviations: Hg Poro = Mercury Porosity, Den = Density log, TG = Natural Gamma log. 8

Figure I. 3: General workflow.....14

Figure. II. 1: Rock column. 20

Figure II. 2: The workflow. 22

Figure II. 3: Rock-forming components. Legend; D.F.=Detrital fragments, F.S=Fine siltstone, CL=Claystone, Car.=Carbonate and dolomite cement, Ab= Albite nests.....24

Figure II. 4: Histograms of the saturated and dry samples (A) and the corresponding box-plots (B).....25

Figure II. 5: Porosity of the rock-forming components.....26

Figure II. 6 : Fracture and convolute structures in the H.U. image and voxel-porosity slices. Red borders in A-B show a calcite filled fracture, whereas red arrows in C-D illustrate an example of a convolute structure in the detrital fragments and siltstone constituent.....27

Figure II. 7: Sequence clustering of voxel-porosity values. 28

Figure II. 8: Box-plot of porosity by clusters; cluster 1 represents the macro-pores cluster, and cluster 2 refers to the Matrix cluster. 29

Figure II. 9: Porosity clusters by rock-forming components. 30

Figure II. 10: Crosstabulation chart table of rock components and clusters. 31

Figure III. 1: Definition of the Representative Elementary Volume, REV (after Bear, 1972). 40

Figure III. 2: The workflow. 41

Figure III. 3: Rock-forming components and boundaries of layers defined. 42

Figure III. 4: The SPC chart. 43

Figure III. 5: An example of the applied ARIMA charts. A – Parameters of the selected model; B – The explicit form of the selected model; C – Parameters of the ARIMA chart; D – ARIMA chart with the indication of the volume step where the REV can be defined. 45

Figure III. 6: Sedimentary features of the defined layers. A – Convolute lamination; B – Mud intraclast; C – Crack; D – Cross-bedding. Red dashed lines show the sedimentary structure out-borders and red arrows point at actual deformation of detrital fragments - fine siltstone.....52

Figure IV.1: A: Definition of the Representative Elementary Volume, REV (after Bear, 1972). B: locations of initial cubic volume.....57
Figure IV. 2: The workflow.....58
Figure IV. 3: Average porosity values of the five rock-forming components; boundaries of layers, and voxel-porosity averages of each layer were also defined.....62
Figure IV. 4: The linear (Pearson) correlation coefficients for averaged porosity cut-off ratios and rock-forming components.....67
Figure IV. 5: Albite nests. On the left, the albite voxels appear with very high CT numbers. The corresponding voxel porosities are shown for the same slice on the right. The red arrows indicate albite removed from pore volumes, and white arrows point to the albite filled pores. 67

List of Tables

Table II. 1: Basic statistical properties of voxel porosity by rock constituents.....27
Table II. 2: Comparison of mean porosity coming from C.T. scans with routine porosity measurements. 32
Table II. 3: Statistical characteristics of the density contrast between the dry and saturated scans and the calculated voxel porosity of the 10 HU absolute value noise.....36
Table III. 1: Averaged compositional data by layers of the CT volumes 46
Table III. 2: The linear (Pearson) correlation coefficients for averaged HU data of rock-forming components. Between brackets, the $p < 0.05$ values indicate statistically significant non-zero correlations at the 95.0% confidence level. 47
Table III. 3: Summary table of REV calculations.....49
Table III. 4: Summary statistics of actual and simulated REV values of clayey-siltstone and fine siltstone layers.....51
Table IV. 1: Summary table of REV calculations.....61
Table IV. 2: Summary statistics of actual and simulated REV values.....63
Table IV .3: Summary statistics of the mean porosities of the REVs.....63
Table IV. 4: Tabulated relative frequencies of the average voxel porosities by layers.....65

1. Chapter I: Introduction

1.1. Boda Claystone Formation; General view

1.1.1. Geological setting: location, lithology, and mineralogy

The Upper Permian Boda Claystone Formation (BCF) is located in the Western Mecsek Mountains (WM Mts), Southern Transdanubia, SW Hungary. The Mecsek Mountains are part of the Tisza Mega unit. This unit, which forms a colossal lithosphere fragment (more than 100,000 km^2), was detached from the southern margin of Variscan Europe during the Jurassic (Haas & Péró 2004; Balla 1987; Horváth 1993) and settled eventually in the Pannonian Basin (Figure I. 1A).

The BCF takes place in two domains in the Western Mecsek Mountains: The Boda block and the Gorica block. Data from boreholes and geological mappings reveal that the extension of BCF is around 150 km^2, and only a 15km^2 outcrop is exposed at the Boda village region in WM Mts.; however, in the Gorica block, exposure of BCF is unseen. Several deep drillings reached the BCF in the Gorica block, but only the borehole Ib-4 (Figure I. 1B) recovers the sequence of BCF in significant thickness (c.a. 200 m). The total thickness of the BCF is estimated to be 700–900 m in the peri-anticlinal structure of the WM Mts (Boda block). In contrast, the overall thickness of the Gorica block does not exceed 350 m. (Jámbor 1964; Barabás & Barabás-Stuhl 1998; Máthé 1998; Árkai et al. 2000; Varga et al. 2005; Lázár & Máthé 2012; Németh & Máthé, 2016).

Stratigraphically, the BCF is delimited by Cserdi and Kővágószőlős conglomerates occurrence. For illustration, the lower boundary of BCF is located where conglomerate intercalations of Cserdi formation disappear, and fine-grained sandstones and siltstones start to dominate. Whereas its upper boundary is marked by the appearance of conglomerates at the bottom of the Kővágószőlős Sandstone formation (Barabás & Barabás-Stuhl, 1998).

The BCF lithology, in short, is characterized by small grains size (clay to silt) beds. It starts with fine-grained sandstone beds at the base; these are overlain by albitic claystone/siltstone, with successive claystone, albitic clayey siltstone, and silty claystone with dolomite at the top. The Green and greenish-grey siltstones and claystone occur

infrequently. Desiccation cracks, dolomite concretions, convolute laminations, and cross-bedding are recognized almost throughout the formation. (Konrád et al., 2010). The stratigraphical position of the core sample studied within the entire cored sections is shown in Figure I. 2.

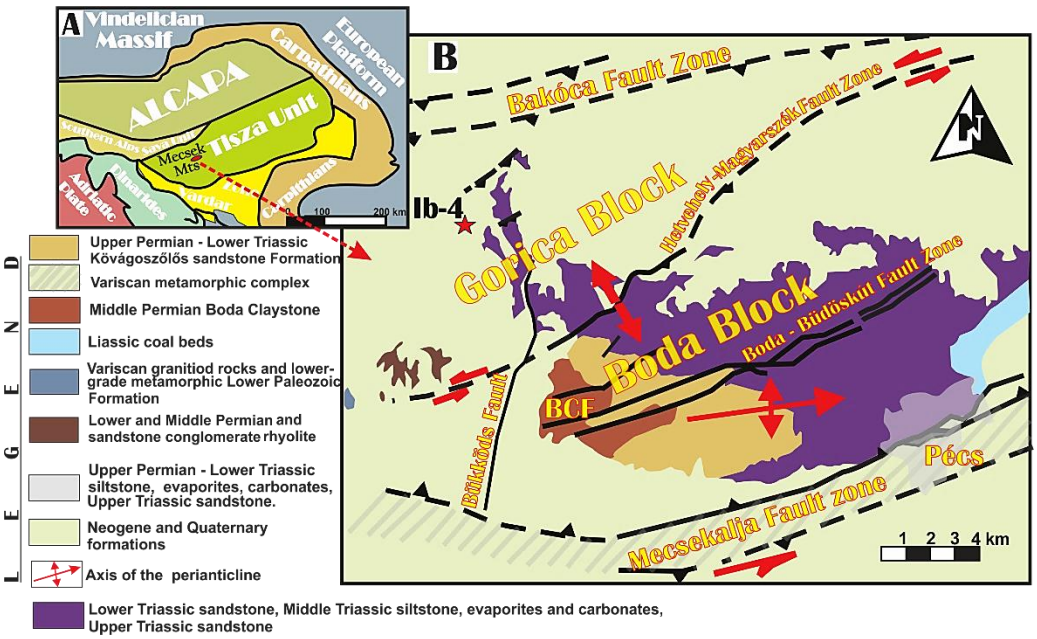

Figure I.1: Distribution of Boda Claystone Formation sequences in the Mecsek Hills area (after Haas & Péró, 2004); B – The studied core site, Ibafa 4 (Ib-4),

The main rock-forming minerals of the BCF are: clay minerals (10–55 wt%), detrital quartz (5–30 wt%), albite (20– 60 wt%), carbonate minerals (calcite and dolomite; 10–50 wt%) and hematite (5–10 wt%) (Máthé 1998, 2015; Árkai et al. 2000; Fedor et al., 2018). The absolute dominant clay mineral is illite–muscovite (15–50 wt%), with chlorite (0–35 wt%) as another determinant clay mineral phase; smectite, kaolinite, vermiculite and mixed-layer clay minerals (illite/ smectite, chlorite/smectite) being identified in minor amounts (Máthé 1998, 2015; Árkai et al. 2000; Varga et al. 2005, 2006). In the greyish black siltstones and claystone interstratification, the illite–muscovite content decreases, and the chlorite becomes the dominant mineral (e.g., Fedor et al., 2018).

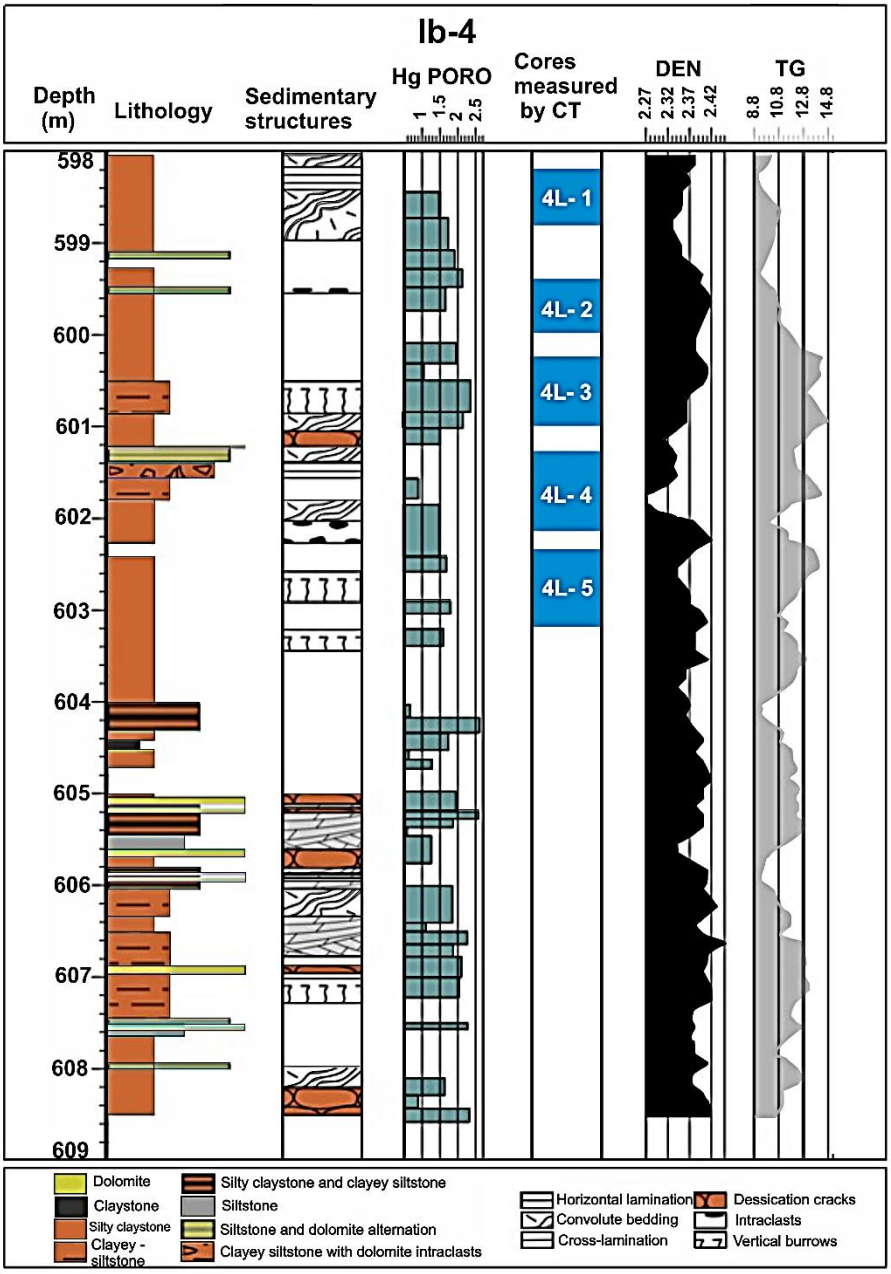

Figure I. 2: The core and the intervals studied by CT. Abbreviations: Hg Poro = Mercury Porosity, Den = Density log, TG = Natural Gamma log.

1.1.2. Depositional environment

Jámbor (1964) was the first to describe the formation and interpret it as lacustrine sediment. The lacustrine basin received only fine-grained sediments, while the surrounding areas accumulated coarser-grained deposits from ephemeral streams (Cserdi Formation (Konrad

et al., 2010). The extreme thickness of the BCF indicates an active fault during the deposition process (Fazekas et al., 1987). Subsidence and basin formation was driven by crustal reorganization and re-equilibration following the compressional phases of the Variscan orogeny (Vozárová et al., 2009). As the BCF was deposited in a closed subsiding basin of a relatively minor extent, possibilities for correlating the formation are limited. No similar coeval sediments are known within the present-day Pannonian Basin (Alcapa, Tisza, and Dacia Units) (Konrad et al., 2010). Therefore, the impact of tectonics on these areas will be difficult to compare (McCann et al., 2008). However, the sedimentary features of the BCF indicate the same aridification of the climate of Pangaea as do other Middle Permian playa sediments that were also deposited in isolated intermontane basins in the Variscan foreland (e.g., Schneider et al., 2006). To summarize, the intermontane basin with playa lakes developed under arid climatic conditions. Most BCF was deposited in a playa mudflat, with intercalations of lacustrine and fluvial origin. The source rocks were granite and rhyolite, so a 'Lake Natron-type' chemical environment was formed. (Konrad et al., 2010).

Otherwise, petrological and geochemical analyses of Boda block, i.e., dominantly albite, crystals of dolomite layers are pseudomorphs after 'Hopper halite, desiccation cracks, and high Na_2O contents, proved that the BCF was deposited in halite- and sulfate-dominated, long-lived perennial and ephemeral inland saline lakes surrounded by saline and dry mudflats and distal alluvial deposits, under semi-arid to arid climatic conditions (Barabás & Barabás-Stuhl 1998; Máthé 1998; Árkai et al. 2000; Varga et al. 2005; Máthé & Varga 2012; Fedor et al., 2018). In comparison, the absence of dolomite layers, analcime dominant, and lacking (pseudomorphs after halite) deposits in Gorica block, suggest that the lake environment was moderately saline-alkaline (Remmy & Ferrell 1989; Máthé 2015).

1.1.3. The importance of Boda Claystone Formation

Detailed analysis of the BCF has been in progress since the late 80s. The so-called Alpha tunnel operated in the mid-1990s was the deepest in-situ underground research laboratory (URL). Laboratory analyses include mineralogical, geochemical, hydrogeological, geotechnical, and tectonism and alteration processes (Kovács 1999). However, only

limited petrophysical measurements were carried out for technical reasons (Szkfi 1990, 1991; Mév 1993; Csicsák 1999). The actual Investigation of the Boda Claystone Formation as a potential rock formation for high-level nuclear waste (HLW) disposal began in 1989 and has continued up to the present. Since 1998 Public Limited Company for Radioactive Waste Management (PURAM), a Hungarian governmental agency, has the responsibility and monetary funds for coordinating studies. In 1999, PURAM announced the BCF as a suitable rock formation for a high-level nuclear waste repository. This is due to a bunch of essential properties of BCF influencing rock radionuclide migration. For instance, it has a massive, homogeneous rock body, significant extension and thickness (700-900), low bulk-porosity (0.6-1.4%), and very low permeability (10^{-11}- 10^{-13} m/s). In addition, the abundance proportions of clay minerals and albite could play a significant role in sorption, sealing, isolation capacity, and adsorption. (Máthé, 1998; Boisson, 2005; Lázár, & Máthé., 2012).

Despite the extensive studies covering most BCF aspects, and in spite of the fact that 3D X-ray computed tomography scans (CT) could efficiently reveal the spatial distribution of the inner structure of objects examined and provide unrivaled information about materials from scale lengths of meters, down to tens of nanometers non-destructively, there is no published studies incorporate the 3D X-ray computed tomography scan analysis to evaluate, i.e., petrophysical properties (e.g. Al-Raoush & Papadopoulos, 2010) of BCF samples. The general purpose of this Ph.D. research, therefore, is to accurately quantify the variability of petrophysical properties, and density of the rock-forming components of a core sample of BCF using CT scan images. Such quantification can make a straight connection between the rock-forming components and variances of voxel- porosity averages. Moreover, CT data would allow for evaluating the heterogeneity of BCF by performing REV analysis (e.g. Borges et al., 2018).

1.1.4. CT principle

X-ray computed tomography (CT) can provide unrivaled information about the internal structure of materials non-destructively from the meters down to the tens of nanometres length scales. It exploits the penetrating power of X-rays to obtain a series of two-dimensional (2D) radiographs of the object viewed from many different directions. This

process is called a CT scan. A computed reconstruction algorithm is then used to create a stack of cross-sectional slices from the object's 2D projections (radiographs) (Withers et al., 2021).

A single CT scan image is produced using a mono-energetic X-ray. As each X-ray beam passes through the sample, it attenuates varyingly, and the transmitted X-ray is received by a detector (Hounsfield, 1973). The attenuation is measured at many angles and reconstructed in a 3D matrix. The 3D distribution of the X-ray attenuation coefficient in reservoir rocks is dependent on variations in mineral composition (atomic number and density), porosity, and saturation. X-ray attenuation is physically determined mainly by photoelectric absorption and the Compton effect. Photoelectric absorption is dependent on the effective atomic number and is especially important at low energies (Yang et al., 2019; Withers et al., 2021). The Compton effect predominates at high energies, and the associated X-ray attenuation is mainly controlled by density (Withers et al., 2021). Just as 2D images are made up of 2D pixels, 3D images are made up of many cubic volume elements called voxels (Withers et al., 2021). The X-ray attenuation can be determined using Beer Lambert's law (Eq. 1). Each rotation of the X-ray source around the sample produces a cross-sectional image, which can then be stacked to form a 3D volume.

$$I = I_0 e^{-(\mu d)} \qquad (1)$$

where I is the intensity of the transmitted X-ray, $\boldsymbol{I_0}$ the initial X-ray intensity, $\boldsymbol{\mu}$ the linear X-ray attenuation coefficient, and $\boldsymbol{d}$ the length of the X-ray path inside the object.

When X-ray energy and intensity are kept constant, linear attenuation of X-ray occurs as a function of density, resulting in the sensitivity of CT images to density changes (Heismann et al., 2003; Duchesne et al., 2009).

Series of X-ray attenuation measurements are numerically processed (reconstructed) to show the spatial distribution of X-ray attenuation coefficients within the sample; the signal at each point in the reconstructed images, referred to as CT numbers, are expressed in Hounsfield units. The Hounsfield unit (HU) scale is a linear transformation of the original linear attenuation coefficient measurement into one in which the radiodensity of distilled water at standard pressure and temperature (STP) is defined as zero Hounsfield units (HU),

while the radiodensity of air at STP is defined as – 1000 HU. The corresponding HU value is therefore given by:

$$HU = 10^3 * \frac{\mu - \mu_w}{\mu_w} \qquad (2)$$

where $\boldsymbol{\mu}$ is the attenuation coefficient of the measured material, and $\boldsymbol{\mu_w}$ **i**s the attenuation coefficient of water. The X-ray attenuation coefficient is represented as CT numbers for a medical CT, which is calibrated to air with the value – 1000 and water with the value 0 according to the Hounsfield scale.

Grey-scale images are generally used to visualize the differences in X-ray attenuation. This process provides a digital 3D grey-scale representation (often referred to as a tomogram). This can be quantitatively analyzed and virtually sliced in any direction, or specific constituents can be digitally color-coded to visualize the 3D morphology. For example, bright colors (high values) have low porosity and dark shades (low values) have high porosity in reservoir rocks with constant mineralogy and saturation (Földes et al., 2004; Wesolowski & Lev, 2005; Földes, 2011).

Measurements with X-ray CT are subject to various errors and image artifacts, including Beam hardening, star-shaped, positioning error, and machine error. Techniques used to minimize them were discussed in full by Van Geet et al. (2000), Ketcham & Carlson (2001), and Akin & Kovscek (2003).

1.1.5. Applied CT scans

A core sample of BCF (Ib-4), about five m-long, was scanned at a high-resolution X-ray CT facility at the Institute of Diagnostic Imaging and Radiation Oncology, University of Kaposvar, Hungary. The instrument operates at 120 kVp (peak kilovoltage), with 250 mAs (milliampere-seconds) current, 1.0 s (sampling intervals). The lateral resolution was (0.1953 x 0.1953) mm2 with 1.25 mm scan-slice thickness. The image reconstruction matrix was 512 x 512 pixels. The field of view (FOV) was approximately 9.99 cm.

Scans were made using a modified dual-scanning approach (Balazs et al., 2018). Usually, rock samples are dried in a vacuum oven at temperatures of 120 to 210 °F (50 to 100 °C). Drying is terminated when the samples reach a stable weight (Soeder, 1986). After six

hours of vacuuming the sample, all pore water was removed, and CT measurements were acquired (scan of the dry core). The next phase was pumping water into the whole dried sample (saturation process). After an hour of relaxation, those slices that went under vacuumed then flooded condition were re-scanned. CT images were stored in a DICOM (Digital and Imaging Communications in Medicine) format.

CT images are stored in a DICOM (Digital and Imaging Communications in Medicine) format. A DICOM file contains in its metadata the scanning parameters and scanned object identification under different attributes. Of these metadata, the *Pixel Spacing* and *Slice Thickness* attributes are important for geoscientific applications as they record the dimension (in millimeters) of each voxel in the x, y, and z-direction. Each CT number can be assigned a real-world distance (or depth), allowing CT number profiles to be constructed so that depth and geometrical measurements can be calculated. DICOM images are be easily read by 'classical' 3D volume rendering software.

The laboratory guaranteed that the DICOM files were free of any artifacts and that during the second scan, the same pixels were measured as during the first one. We have calculated the porosity values for each voxel of the image slices from both dry and flooded scans (Moss et al. 1990).

1.2. Aims and general workflow

In this work, an X-ray computed tomography (CT) technique is employed to acquire high-resolution 3D images from the 5m core sample. The study objectives recapitulate into five prominent points: 1) calculate and visualize the voxel porosities of each rock-forming component. 2) classify the porosities of voxels into the optimal number of clusters. 3) define rock-forming components by porosity clusters and visualize their distributions. 4) quantify and evaluate the minimum volume of a core sample of the BCF that captures a representative quantity of its physical heterogeneity (i.e., density). Finally, 5) assess the minimum volume of a core sample of the BCF that can evaluate a representative quantity of its petrophysical heterogeneity (i.e., voxel porosity).

Due to the cooperation between the University of Szeged, Geochem Lab., and the Public Limited Company for Radioactive Waste Management (PURAM), the raw data sets of

vacuumed dry and saturated CT measurements of the BCF core sample were transferred to the University of Szeged for further analyses application. Only the texturally intact, unbroken parts of the scanned sample were used. Five CT volume bricks of the core sample thus served as the basis of the present work (Figure I. 3).

A 3D-nearest neighbor algorithm was used to build the 3D volumes of the five scanned core bricks. This process resulted in two Hounsfield lattices, one for the vacuum dried and one for the saturated core volumes. Determine HU intervals and calculating the relative percentages of the rock-forming components for the dry-vacuum scan was necessary for determine the dominant rock-forming components and lent the name of the rock type.

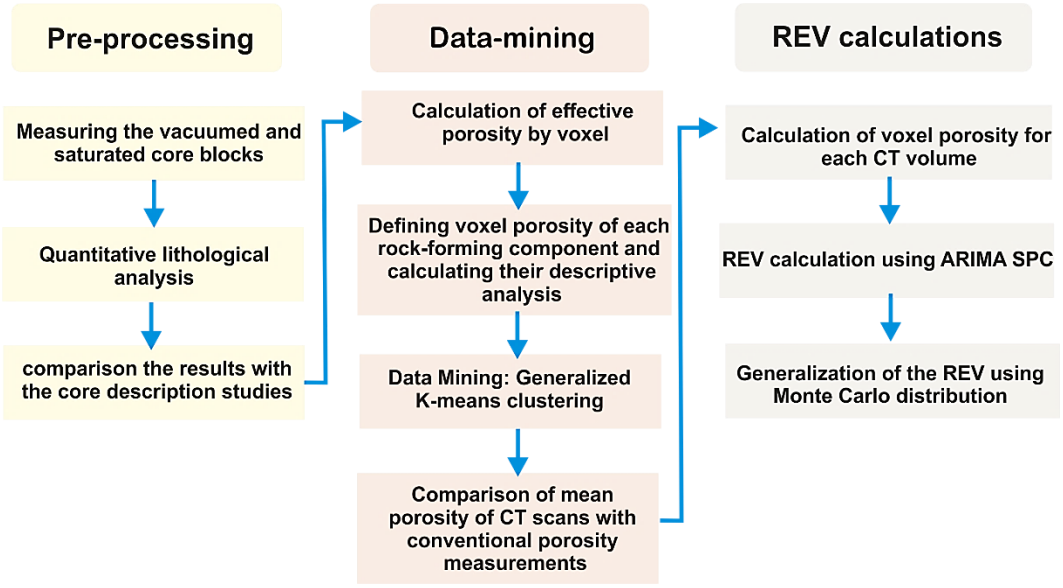

Figure I. 3: General workflow.

The voxel porosities of the scanned slices were computed from both lattices by normalizing the results of the dual scans subtraction via flooded HU values (Moss et al., 1990, Hove et al., 1988). Each voxel of the 3D CT volume was accordingly described with three variables: dry CT number, saturated CT number, and voxel porosity.

The spatial patterns of the voxels with similar effective porosity and textural characters were assorted by a generalized k-means clustering algorithm of data-mining techniques. A

hypothesis test, then, has been applied to evaluate and compare the implemented CT pore measurements with other conventional lab measurements, such as helium and mercury (Full details are in chapter 2).

Representative Elementary Volume (REV) was efficiently utilized in quantifying the inhomogeneity of CT densities of rock-forming components of the Boda Claystone Formation. The REV calculation was established using the Autoregressive Integrated Moving Averages, Statistical Process Control (ARIMA SPC) method. The REV calculations, in brief, were initiated with a single-voxel starting point, in which dimensions were increased symmetrically in all directions. The averages of the acquired (physical interest property i.e. density) values were then plotted on a Statistical Process Control (SPC) chart. Control limits are the standard deviations above and below an SPC chart's centreline; they are named (UCL) for the upper and (LCL) for the lower centreline. If the voxel density measurements are within the tolerance margins of the control limits, then the plotted density values are distributed non-randomly, and the process is in control. Otherwise, plotting the data points outside the tolerance margins would have a random, out-of-control distribution.

The aforementioned process was also applied to study the REV of voxel porosity. Since the REV heavily relies on the spatial position of the initial volume, five different starting positions were pointed out. The ARIMA SPC, therefore, was five times iterated. Each time the initial voxel volume started from a new position in the BCF core sample (upper left, upper right, lower left, lower right, and middle). Consequently, we could compare the averages of the computed REVs and determine the adequate starting point position for REV calculations.

Monte Carlo simulation was used to simulate the long-run properties of REV and the normalized REV of both HU-density and voxel-porosity assessments. Specifics of the ARIMA SPC method are found in chapters 3 and 4.

Chapter II:

Evaluation of 3D small-scale lithological heterogeneities and pore distribution of the Boda Claystone Formation using X-ray Computed Tomography images (CT)

Saja M. Abutaha

The University of Szeged, Department of Geology and Paleontology; 6722, Szeged, Egyetem utca 2-6, Hungary.
Emails; sajaabutaha@geo.u-szeged.hu

János Geiger

The University of Szeged, Department of Geology and Paleontology; 6722, Szeged, Egyetem utca 2-6, Hungary.
Emails; matska@geo.u-szeged.hu

Sándor Gulyás

The University of Szeged, Department of Geology and Paleontology; 6722, Szeged, Egyetem utca 2-6, Hungary.
Emails; gulyas.sandor@geo.u-szeged.hu).

Ferenc Fedor

GEOCHEM Ltd, 55/1 Viola str., Kozármisleny, H-7761, Hungary.
Email; fedor.ferenc@geochem-ltd.eu

Geologia Croatica Journal

74/3 | 305–318 (2021)

DOI: 10.4154/gc.2021.17

2. Chapter II: Evaluation of 3D small-scale lithological heterogeneities and pore distribution of the Boda Claystone Formation using X-ray Computed Tomography images (CT)

By Saja M. Abutaha, János Geiger, Sándor Gulyás, Ferenc Fedor

2.1. Introduction

Since its invention in the 1970s, X-ray computed tomography (CT) has spread and developed quickly, mostly stimulated by growing medical needs for diagnostic procedures and interventions. This technique which was initially meant to provide high-resolution non-destructive 3D reconstructions of bones and soft tissues, eventually attracted interest from other domains such as industry and the geosciences (e.g., Garvey & Hanlon, 2002; Louis et al., 2007). Although computerized X-ray tomography (CT or CAT scanning) has been used in the medical field for more than two decades (Hounsfield, 1973; Ledley et al., 1974), recently, it has been widely adopted in studying earth system processes such as earthquakes, orogeny, basin tectonics, or fluid circulation involving mechanisms down to the scale of individual grains (micrometre–millimetre). The ability of X-ray CT to monitor these mechanisms non-destructively and in three dimensions in the laboratory makes it an ideal tool for geoscientists (Sutton et al., 2002). The X-ray CT has been used in different fields of geosciences, such as studying microstructural and rock physical properties of geological media, aiding and enhancing production in petroleum geology or assessing soil contamination or waste repository issues in environmental geology (Van kaick & Delorme 2005; Cnudde et al. 2006).

CT enables the analysis of the interior features of core samples, including bedding features, sedimentary structures, natural and coring-induced fractures, cement distribution, small-scale grain size variation, and density variation (Coles et al., 1991; Coles et al., 1998). This method has a wide application in geosciences, including analyses of the complex porosity and pore geometry of carbonate reservoirs (Purcell et al., 2009), rock-fluid analysis (Pyraknolte et al., 1997; Purcell et al., 2009; Wennberg et al., 2009), the performance of diverting agents in unconsolidated sandstones (Vinegar and wellington, 1987; Ribeiro et

al., 2007a), and many other topics. For instance, Bonner et al. (1994) confirmed fluid migration in rocks by X-ray CT. Verhelst et al. (1995), Geiger et al. (2009) applied the technique to characterize small-scale heterogeneities in intact samples. Schwartz et al. (1994) modeled the fluid flow in porous rocks by combining theoretical simulations with 3D imaging of the material studied. Additionally, according to the considered rock type, accurate permeability and conductivity estimations are possible using CT (Fredrich et al. 1993; Coker et al. 1996; Coles et al. 1998; Arns et al. 2001,).

Micro-CT (μCT) systems offer a new depth of information that has not been available with conventional two-dimensional microscopy analysis. Several studies have investigated the application of μCT in mineral characterization, including pore analysis (Yang et al., 1984; Vinegar & Wellington, 1987; Withjack, 1988; Hove et al., 1988; Sprunt et al., 1991), liberation and grain exposure (Coles et al., 1991; Spanne & Rivers, 1987; Nichols et al., 1989; Jones et al.,1991; Lontoc-roy et al., 2005; Nahmani et al., 2005), as well as mineral segmentation analysis (e.g., Flannery et al., 1987). The main challenge in the full adoption of a μCT system in these studies lies in the demanding computational processing of a large 3D dataset. Additionally, since most of the μCT analyses are based on the attenuation of the minerals, the presence of minerals with similar attenuations limits the capability of μCT in mineral segmentation (Guntoro et al., 2019). So, although the resolution of a medical CT is much lower than that of the μCT, correspondence between the scales of medical CT measurements and petrophysical, sedimentological measurements applied to core samples makes it better suited for general core sample investigations (Geiger et al., 2009).

The present study focuses on quantifying and evaluating density and porosity characteristics of a core sample using medical CT scans at the scale of a hand-size specimen. A porosity dataset is derived for the identified depositional units from two CT scans at the same location, dry and saturated. This dataset provides porosity information at a much higher resolution, the scale of voxels, compared to traditional petrophysical measurements yielding data for the entire sample as a whole. Coupled processing of information on rock-forming components with pore volume percentages on the same volume (Voxel) has a major advantage over traditional petrophysical approaches. This approach makes a straight connection between the presence and share of rock-forming

components and the expected variances of petrophysical properties. Specific objectives could be addressed as follows: i) Identification of the rock-forming components in the studied CT volumes. ii) calculation of the voxel porosity of the rock-type constituents. iii) analysis and visualisation of the 3D voxel porosity values for each rock component. iv) classification of the voxels into the optimal number of clusters where each cluster has a unique 3D pattern. v) analysis and visualisation of the 3D clusters of voxel-porosity for each rock type. vi) comparison of the mean voxel-porosity with other conventional porosity measurements.

2.2. Analyses workflow

All the CT scans were carefully processed to avoid artifacts such as beam hardening which occurs when the attenuation along a path passing through the centre of the object becomes larger than the attenuation along the path passing through the objects' marginal parts. This happens because lower-energy X-rays are attenuated more readily than higher-energy X-rays; a polychromatic beam passing through an object preferentially loses the lower-energy parts of its spectrum. The result is a beam that has higher average energy than the incident beam, though diminished in overall intensity. This also means that, as the beam passes through an object, the effective attenuation coefficient of any material diminishes, thus making short ray paths proportionally more attenuating than long ray paths. In X-ray CT images of sufficiently attenuating material, this process generally manifests itself as an artificial darkening at the centre of long ray paths and a corresponding brightening near the edges. Beam hardening can be a pernicious artifact because it changes the CT value of a material (or void) depending upon its location in an image. Thus, to eliminate beam hardening, we remove the image's outer edges and analyze only the centre.

A 3D nearest neighbour algorithm was applied to build the 3D volumes of the scanned dry (vacuumed) and saturated core. This algorithm arranged the CT scans' grid systems below one another in the actual stratigraphic position and fully honoured the measured CT numbers. From the dual CT scans, three parameters were available in each voxel: CT number of the dry (vacuumed) state, CT number of the saturated state, and the calculated effective porosity (Figure II. 1). The total number of voxels in each 3D model (dry core, saturated core, and effective porosity) was around 13 million.

The workflow applied in this study relied on three fundamental scopes. The first one was identifying rock constituents according to the pre-classified CT intervals taken from the PURAM

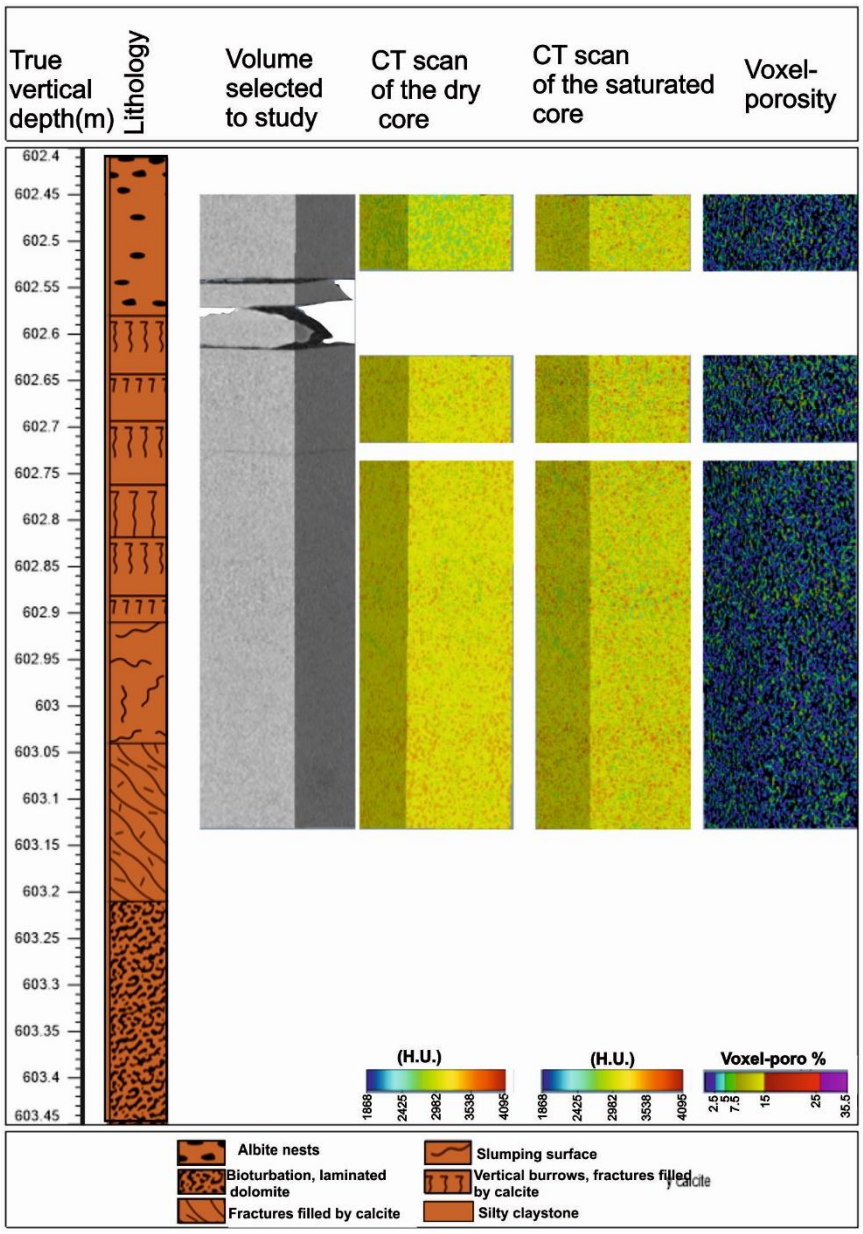

Figure. II. 1: Rock column.

project. In this calibration phase, the suggested CT intervals of the rock components were visually compared with the dry HU patterns of the 3D CT volume; definable geometric characteristics (i.e., sedimentary structures) were also detected ("Pre-Processing" in Figure II. 2).

Each voxel of the 3D CT volume was described with three variables: dry CT number, saturated CT number, and effective porosity. In our view, the dry and saturated CT numbers characterize the rock texture voxel by voxel, and the voxel porosity calculated in each voxel describes the petrophysical characters of each voxel partially. The spatial patterns of the voxels with similar effective porosity and textural characters (dry and saturated CT numbers) were divulged by a generalized k-means clustering algorithm of data-mining techniques ("Data Mining" in Figure II. 2). In this process, we searched for the minimum number of "genetic groups". Classifying CT numbers into the minimum k number of disjoint clusters is an iterative method that assigns each point to the cluster whose centroid is the nearest. Euclidean distance is generally considered to determine the distance between data points and the centroids. K-means clustering algorithm depends on the random choice of initial centroids. The computational complexity of K-means algorithms is very high, especially for large data sets. To determine the stable number of clusters, the K-fold cross-validation technique was used. Each time, one of the k subsets is used as the test set/ validation set, and the other k-1 subsets are put together to form a training set. The error estimation is averaged over all k trials to get the total effectiveness of our model. The recent approach significantly reduces bias as we are using most of the data for fitting which significantly reduces variance.

The final, third phase includes post-processing. The HU intervals of rock-type components coming from the first phase were used to build up the Boolean lattices for each textural component. These Boolean lattices were utilized to show the 3D spatial distributions of voxel-porosity by rock type (by multiplication of Boolean lattices with voxel porosity) and the 3D distribution of porosity clusters by rock components (by multiplication of Boolean lattices with clusters' porosity).

Lastly, descriptive analyses were employed to estimate the statistical measure of central tendency and dispersion to organize the pores voxel information for each rock constituent in each HU 3D brick volume. A hypothesis test has been applied to evaluate and compare the implemented CT pore measurements with other conventional lab measurements, such as helium and mercury measurements.

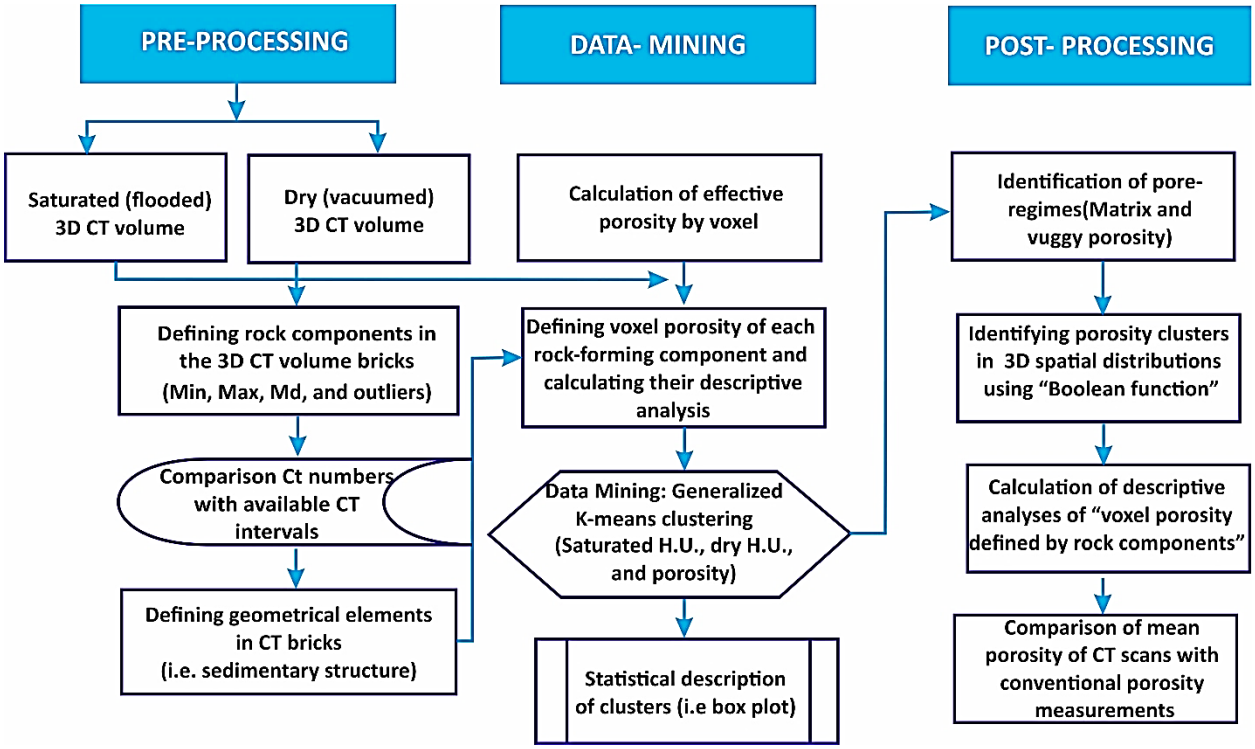

Figure II. 2: The workflow.

2.3. Results

2.3.1. CT characters of rock-forming components in the studied core.

After the CT numbers calibration and clearing beam hardening, the intervals from PURAM's study were linked with the actual geological information of the core sample to visualize the 3D rock-forming components distribution.

Each 3D brick of the dry scans includes 5 rock constituents (Figure II. .3); detrital fragments shown as black (HU <=2700), fine siltstone in grey (2700 HU-3150HU), claystone with green (3150HU-3300HU), dolomite, and calcite cement appears in light orange (3300 HU-3600 HU), and Albite has a dark orange colour (HU>3600). A set of structures could also be identified, for instance; the upper first partition of the lithology profile in (Figure II. 4) shows albite nests; it appears in the first 3D volume brick. The vertical burrows and calcite-filled fractures are dominant throughout the second and upper

third profile's partitions. The middle part of the bottom lithological profile shows some slumping surfaces.

The bivariable histogram in Figure II 4A shows both saturated and dry core HU frequency observations. The midst bins intervals of the fine siltstone and claystone components (2700-3300 HU) pointed out the higher dry HU observations than saturated ones. In contrast, the intervals corresponding to carbonate and albite nests (>3300 HU) are characterized by higher HU values of the saturated sample. The coarse siltstone intervals(2700-2400) display, again, greater HU frequency observations in the saturated than in the dry core.

Figure II..4B shows box-plot charts of the HU values for the dry and saturated core sample. The dry core's median is around 3100, while the saturated one is slightly lower than this. The first quartile (lowest 25%) of dry and saturated HU values are similar, at about 3200. the third quartiles (75% mark) are 3250 and 3000 HU for the dry and saturated core samples, respectively. The HU saturated chart's minimum value is 2550, and the maximum is 3700. Likewise, the minimum dry core HU value is 3175, and the maximum one is 3200. Plenty of high and low HU value outliers can be found in the saturated core sample volume; however, no outliers have been noticed in the dry one. The increased height of the box of the HU saturated core volume indicates the greater variation dispersed data, while the decreased height of the HU dry volume box indicates the less dispersed data. As shown by the extreme outliers' values at the end of the two whiskers of the HU saturated core volume and the larger ranges, the overall spread indicates the wider distribution and more scattered points.

2.3.2. 3D Spatial patterns within the core

The first 3D volume profile's bricks of the detrital fragments' porosity in Figure II. 5, have 2881384 voxels; 21916 of these porosity values are greater than zero. The porosity mean of the terrigenous detrital fragments is 0.16%, with a high coefficient of variation value reaching 1039.39%. However, the fine siltstone component has 8,006,806 of no null voxel porosity value from the overall voxels number (8,655,548). Its mean porosity is 3.39%, and the coefficient variation is 134.99%.

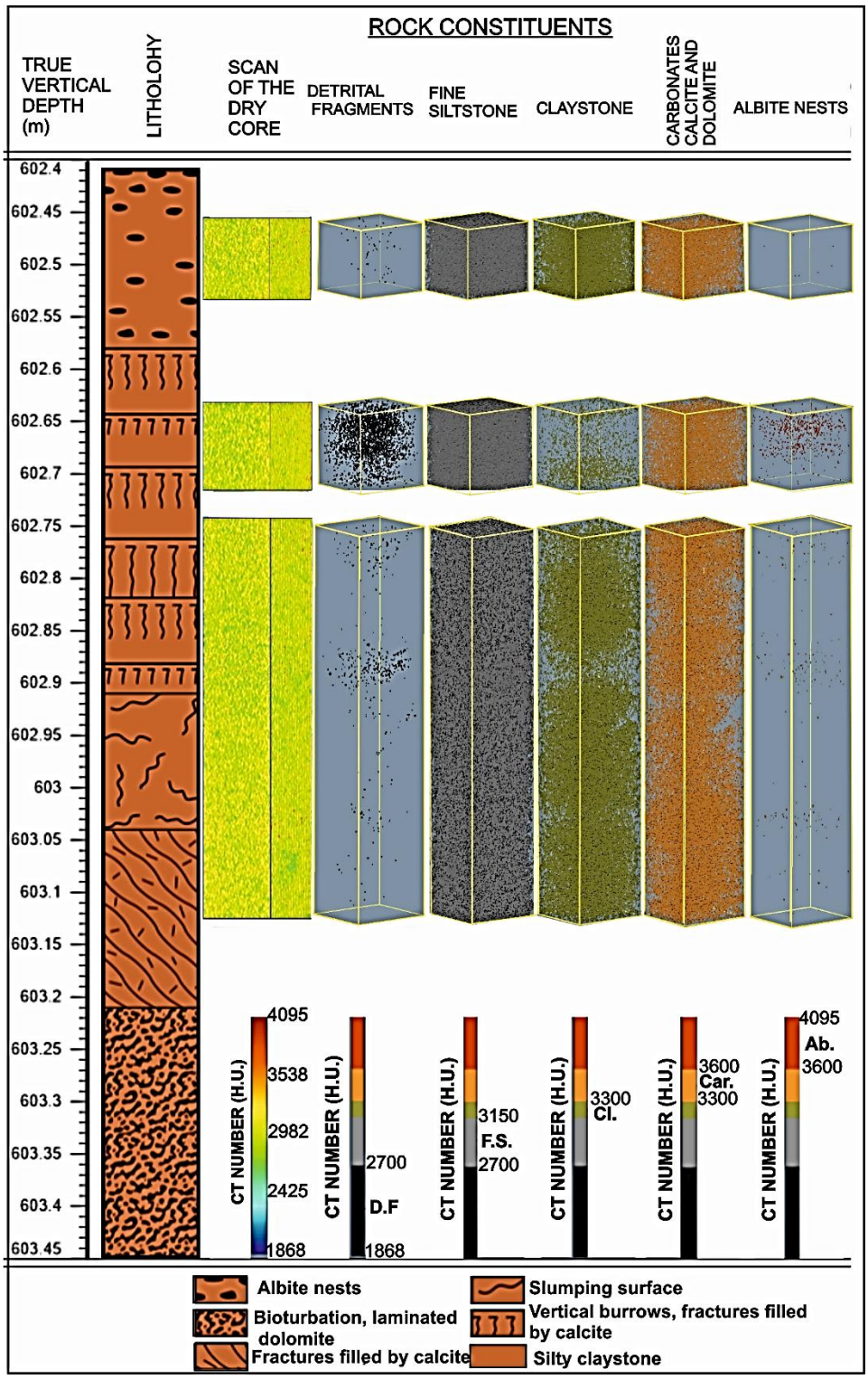

Figure II. 3: Rock-forming components. Legend; D.F.=Detrital fragments, F.S=Fine siltstone, CL=Claystone, Car.=Carbonate and dolomite cement, Ab= Albite nests.

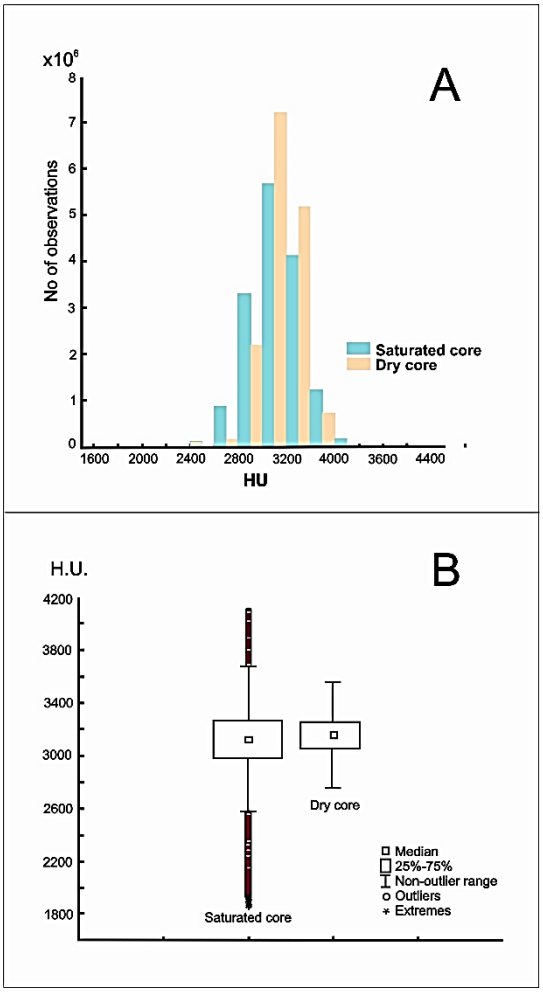

Figure II. 4: Histograms of the saturated and dry samples (A) and the corresponding box-plots (B).

The claystone component includes 6238159 porosity voxels; 5540873 are not null (porosity values >0). The porosity voxels mean and the coefficient of variation of the claystone component is 1.10% and 1.21%, respectively.

The carbonate component consists of 4052229 voxels; 3500052 of the porosity voxels values are larger than zero. The mean of carbonate porosity voxel is 0.24%, with the second higher coefficient value of 458%. The albite nests component has 2857049 voxels; only 177 of them have no null porosity values. The mean porosity voxels of the albite nests are 2.14%. And the coefficient of variation is 77.39%. Further details of porosity basic statistical properties by rock constituents are illustrated in Table II. 1.

The conspicuous sedimentary structures in the CT images; fractures, and convolute deformation are marked in Figure II. 6. Fracture in Figure II. 6A shows high-density contrast between the calcite's infilling material and surrounding sediment. It is recognized as dark parts in the porosity CT image (Figure II. 6B). Conversely, the convolute lamination textural pattern has almost been preserved in the CT porosity scan image (Figure II. 6C-D).

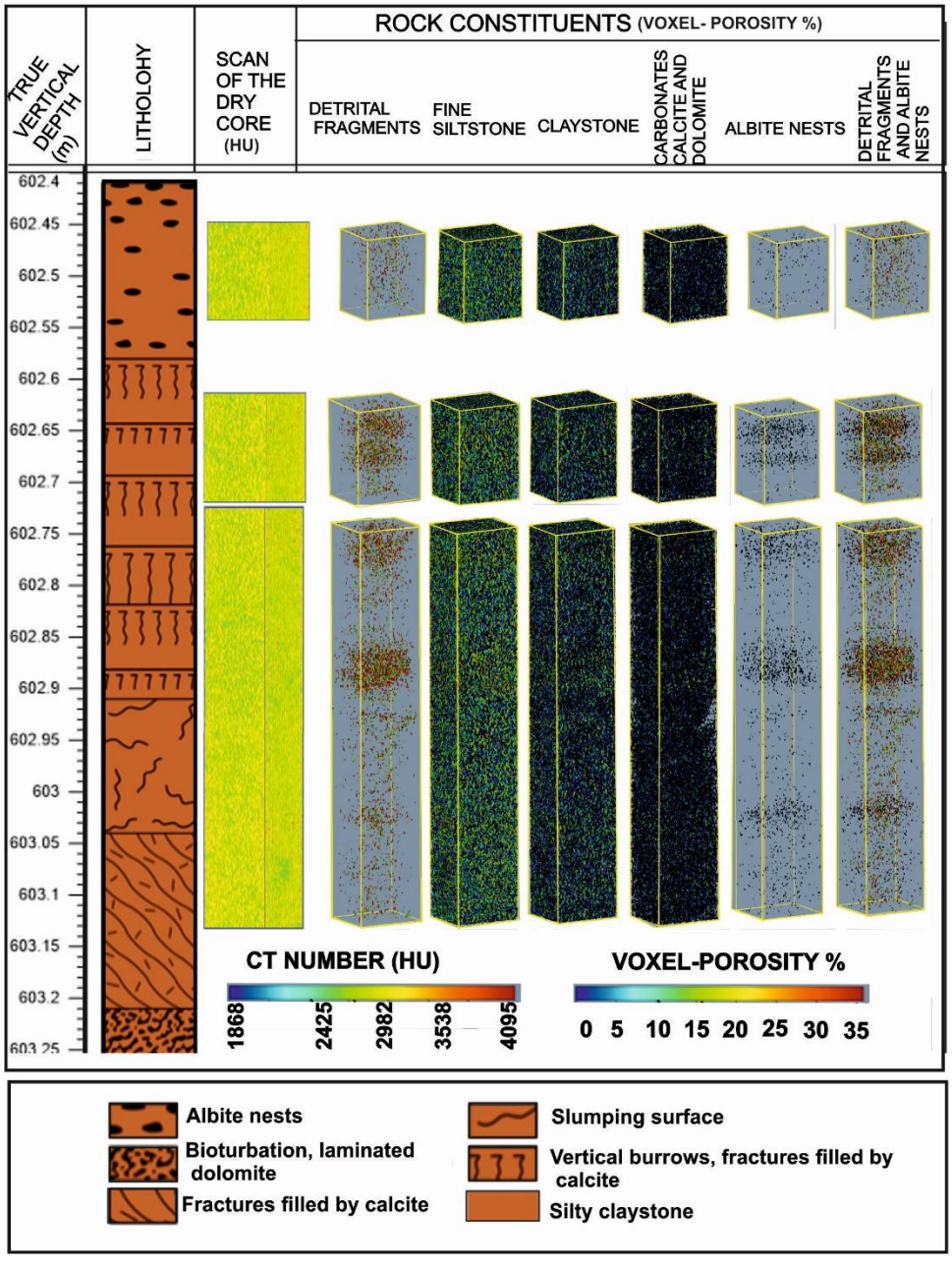

Figure II. 5: Porosity of the rock-forming components.

Table II. 1: Basic statistical properties of voxel porosity by rock constituents.

		No. of voxels	No. of No-null voxels	Mean of voxel porosity %	Min. of voxel porosity %	Max. of voxel porosity %	Coefficient of variation %	Min. voxel porosity of outliers %
Rocks constituents	**Detrital fragments**	2881384	21916	0.16	0.0004	35.74	1039.39	32.33
	Fine siltstone	8655548	8006806	3.39	0.0007	33.11	134.99	15.14
	Claystone	6238159	5540873	1.1	0.0005	23.08	221.12	1.21
	Carbonate	4052229	3500052	0.24	0.0006	19.24	457.34	2.10E-12
	Albite nests	2857049	117	2.14	0.055	7.54	77.39	5.73

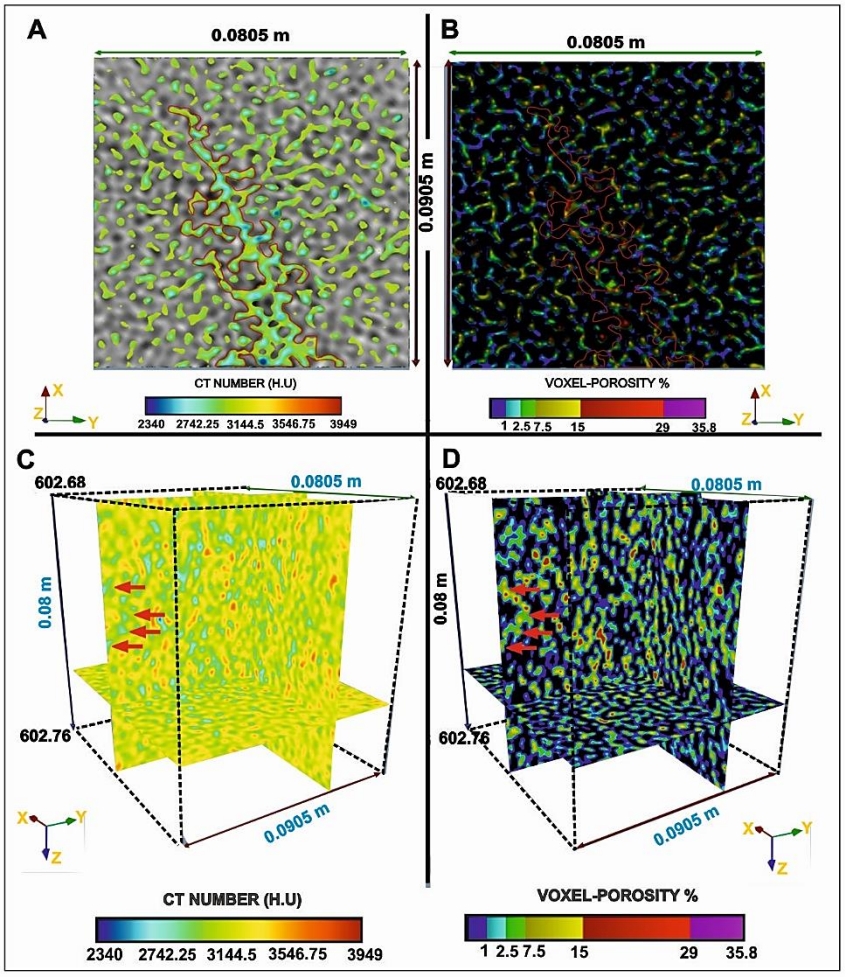

Figure II. 6 : Fracture and convolute structures in the H.U. image and voxel-porosity slices. Red borders in A-B show a calcite filled fracture, whereas red arrows in C-D illustrate an example of a convolute structure in the detrital fragments and siltstone constituent.

Textural variables of the HU of the saturated core (FLD) and HU of the dry core, as well as the porosity variable for petrophysical properties, were utilized to detect textural and petrophysical voxel characteristics using the genetic groups' technique. Our work deals with Chebyshev distances; 10 (v-value) cross-validation and 20 iterations were applied in each approximation. There were about 13 288 316 training cases (Figure II. 7). The initial result of clustering was 6 clusters, k=6 (Figure II. 7 A). However, the arithmetic means of porosity manifest that Clusters 1, 3, and 6 are quite similar; clusters 5 and 2 are also comparable. Therefore, the maximum number of porosity clusters for the next run was suggested to be 3, and the minimum number of clusters premised to be 2, K=3 (Figure II. 7 B). Eventually, two clusters were demonstrated for genetic heterogeneity of the porosity values greater than zero, K=2 (Figure II, 7 C).

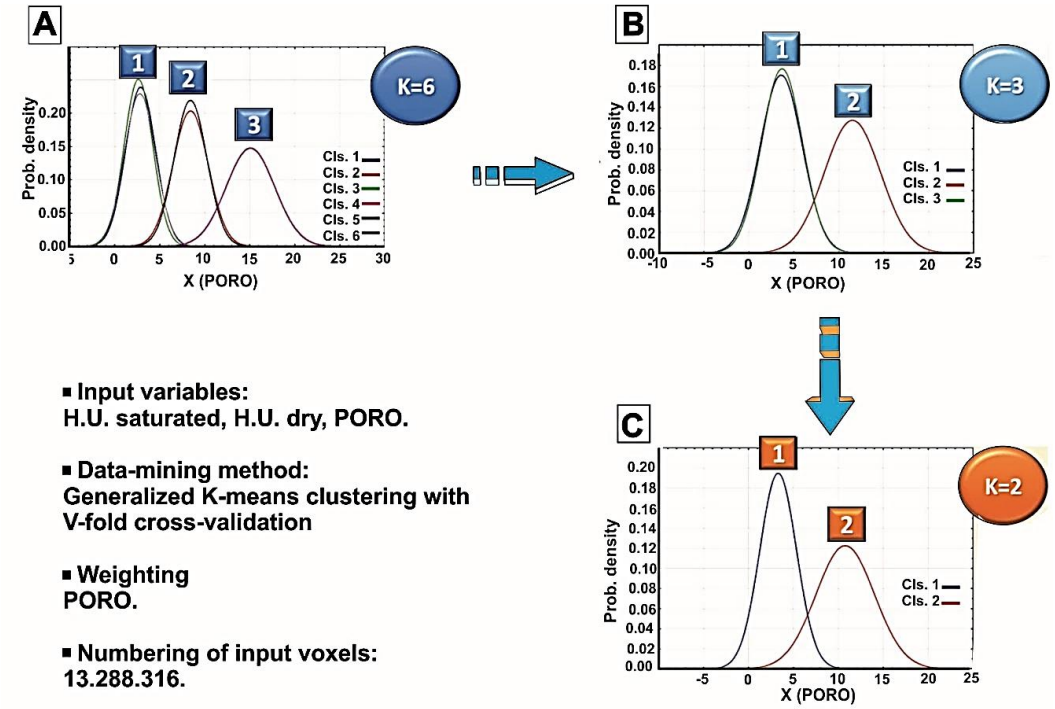

Figure II. 7: Sequence clustering of voxel-porosity values.

To compare the spread and centers of porosity values larger than zero for the two resultant clusters, the box-plot chart was used (Figure II. .8).

The median of cluster 1 appears to be approximately 10%, whereas cluster 2 has a median of around 2.5%. 25% of cluster 1 porosity values are less than 8%. Hence, 75% of the porosity values in cluster 1 are larger than 8% and lower than 19% (IQR range=11%). In comparison, 25% of porosity values in cluster 2 are less than 1%. Thus, 75% of voxel porosity in cluster 2 is higher than 1% and lower than 8% (IQR range=7%). Therefore, the above two clusters could be presented by their average porosity values; matrix porosity with an average of 2.5%, and macro-pore porosity with a 10% average. The porosity outlier values beyond the upper whisker in Figure II. 9, are an exclusive macro-pores cluster note. The outlier values are extended from 18% (over the maximum value) up to 37% (extreme outlier).

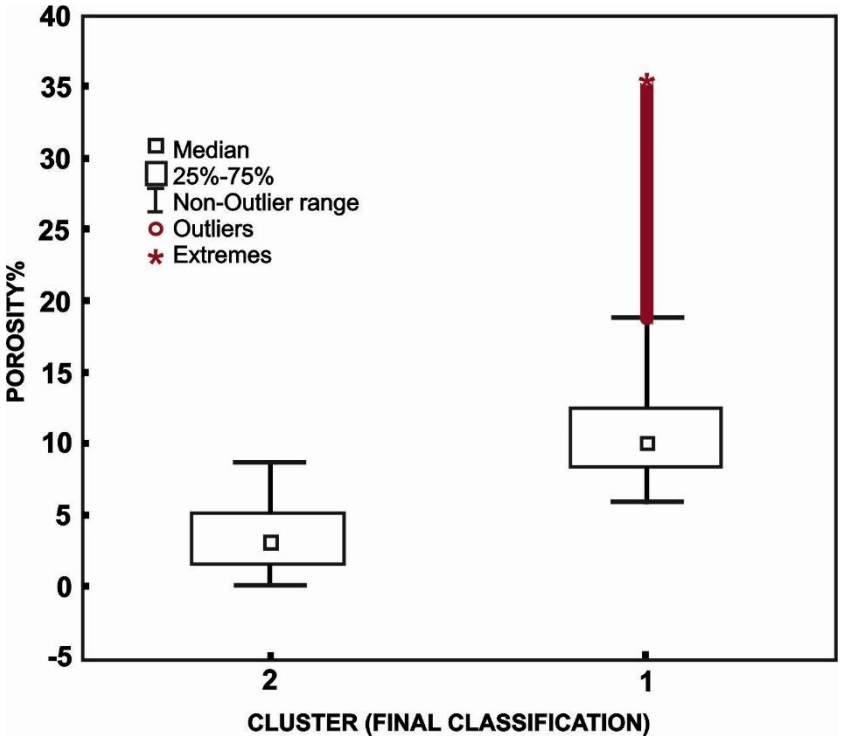

Figure II. 8: Box-plot of porosity by clusters; cluster 1 represents the macro-pores cluster, and cluster 2 refers to the Matrix cluster.

Figure II. 9 shows the 3D distributions of the three porosity clusters for each rock constituent. Clusters are identified in three colours; black for no porosity, green for cluster 1 (Matrix porosity cluster), and cluster 2 has a red colour (macro-porosity cluster). The detrital fragments component shows almost a mixture of the three colours. The cluster of

no porosity is prevalent in the fine siltstone component, while clusters 1 and cluster 2 are less abundant.

The pervasive cluster in the claystone component is the no-porosity cluster with the subdued appearance of cluster 1. Carbonate/dolomite and albite constituents show mostly no-porosity clusters.

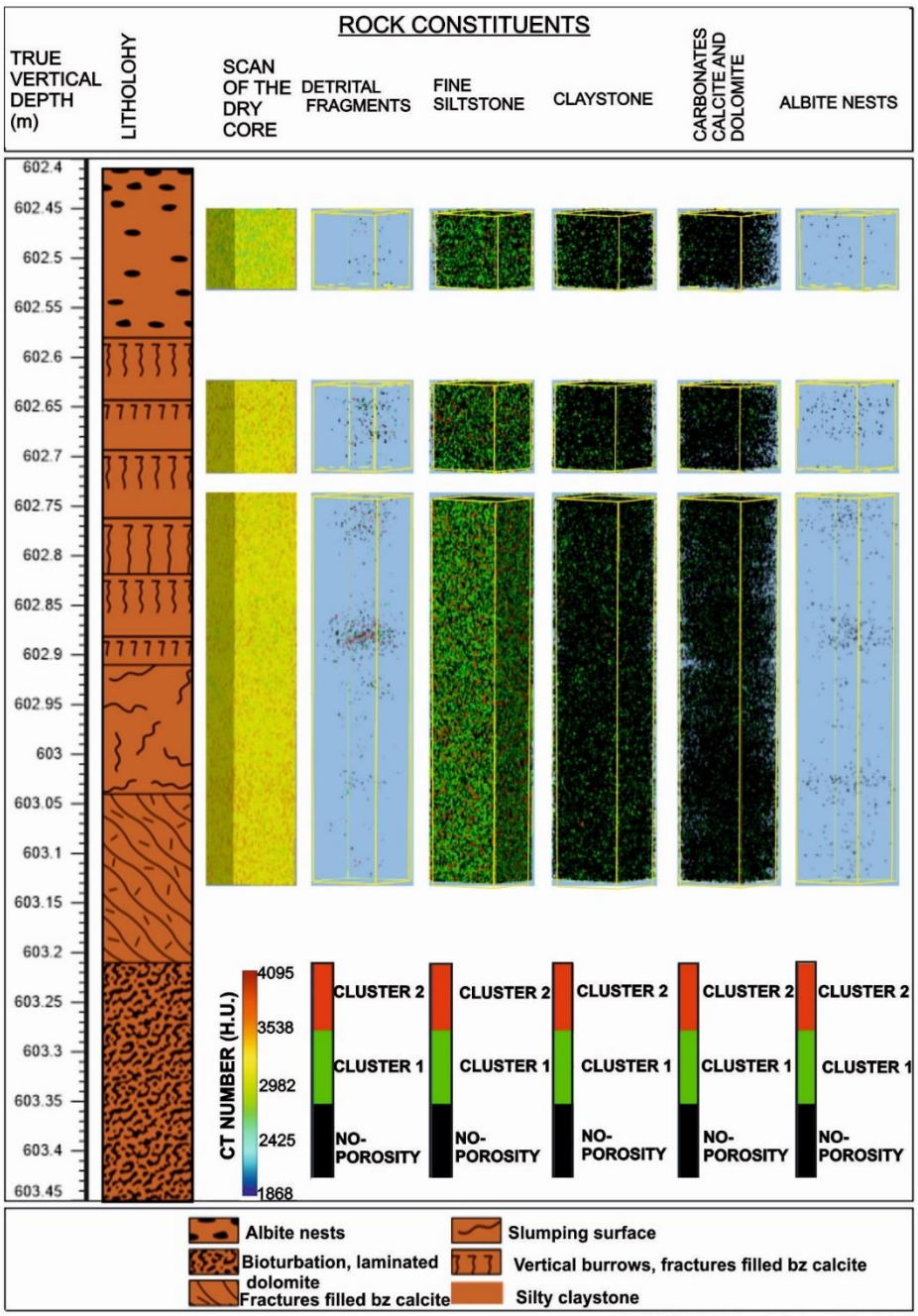

Figure II. 9: Porosity clusters by rock-forming components.

The rock constituents ratios versus porosity clusters distribution are summarized in (Figure II. 10)which shows that each porosity cluster has different rock-forming components in definite ratios. The no-porosity cluster shows a very dense texture, including a variety of rock components; it consists of about 19% fine siltstone, 23% Claystone, 13% carbonate, 0.16% albite, and is almost lacking detrital fragments. Compared with cluster 1, the fine siltstone forms around 20%, claystone is decreased to 8.44%. The carbonate content is also reduced to 1.66%, with no albite, and the detrital fragments component appears as 0.05%. Cluster 2 involves around 12% fine siltstone, 2.33% claystone, 0.27% carbonate, and no albite. The detrital fragment increases to 0.23%.

The total ratios of voxel porosity in each rock component over the three clusters are as follows: 0.29% detrital fragments, 50.74% fine siltstone, around 34% claystone, and 15% carbonate. Albite has the lowest porosity ratio summation along with three clusters at 0.17% (Figure II. 10).

Table II. 2 shows the means of voxel porosity for three clusters; the matrix cluster has a 3.39 mean value, whereas the macro-pores cluster has a 10.77 mean value and zero for the no-porosity cluster. Ratios of voxel-porosity of the three clusters have also been calculated and listed in Table II. 2; the matrix cluster forms 30.37%, the macro-pores cluster accounts for 14.65%, and the no-porosity cluster represents around 55% of the gross clusters' ratios.

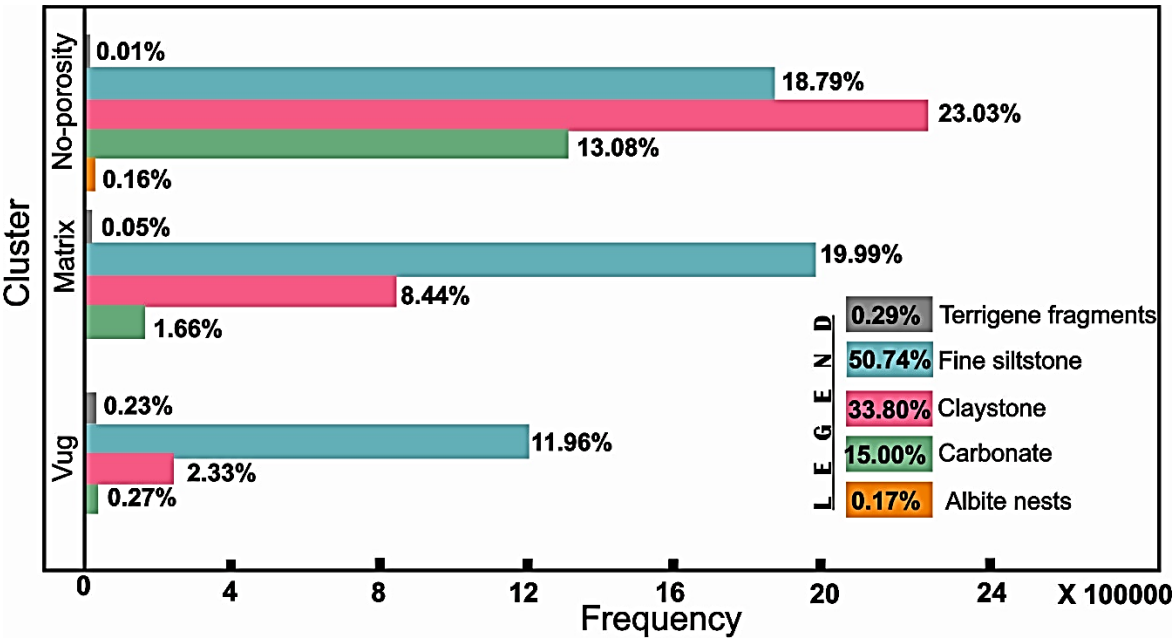

Figure II. 10: Crosstabulation chart table of rock components and clusters.

Table II. 2: Comparison of mean porosity coming from C.T. scans with routine porosity measurements.

	Mean of voxel porosity where poro.>0 (C1)	No of voxels (%) C2	The ratio of voxels (%) C3	Porosity in the full volume (%)		
				From CT scans (C1*C3/100) for macro and matrix	He-porosity	Hg-porosity
Matrix	3.3	4035718	30.37	1.002	-	1.59
Macro-pores	10.77	1946183	14.65	1.578	-	-
Matrix and macro	5.72	5981901	45.02	2.575(*)	2.51	2.02
No-porosity	0	7306394	54.98	0	-	-

The weighted porosity average of matrix and macro clusters in the full volume was calculated by multiplying the total voxel count (C1) for each cluster, by the ratio of voxel porosity of these clusters (C3). Results were arithmetically adding and resulted in a value of 2.58% (Table 1). The final average number reflects each observation's relative importance and is accordingly more descriptive than a simple average. In comparison, the He porosimetry measurements show quite close value for the calculated porosity mean of the CT scans image (2.51%) while the Hg measurement given smaller porosity mean values at 2.02%. More detailed data can be seen in Table II. 2. The Hg and He measurements were carried out in the Geochem Laboratory and the results published in Fedor et al., 2018.

2.4. Discussion

The various illite and illite/smectite mixed assemblages represent the dominant clay minerals of the Boda claystone Formation (Németh & Máthé, 2016). Clay minerals are present in the form of a detrital matrix or as part of rock fragments known as "allogenic clays" as well as replacements (by alterations) or cement, called authigenic clays. Authigenic clay minerals impact formation porosity to a greater extent because of their direct vulnerability to pore fluids compared to detrital clay minerals, which are tightly packed in the rock matrix. Authigenic clay minerals occur as pore linings, pore fillings, pseudomorphic replacements, and fracture fillings (e.g. Ahmad et al., 2018). The reactions of water with these clay minerals (during the core sample's saturation phase) significantly impacted the petrophysical properties. These reactions cause dissolution,

precipitation, plugging, clay swelling, and migration of fine particles. The porous medium of siltstone and detrital fragments can be represented as a network, consisting of pores connected by throats or narrower pore channels. The presence of clay minerals as a dispersed matrix in the pore space reduces the pore throat size and overall permeability due to the release of clay particles from pore walls and their subsequent redeposition downstream in the pore throats, which presumably results in plugging of the pore throats (Al-yaseri et al., 2015; Hayatdavoudi & Ghalambor 1996; Simon and Anderson 1990; Zhou et al. 1995).

The variations of the HU observations in Figure. II 4A could be assigned to the release of fine grains of non-clay minerals (such as carbonate or albite cement) and clay particles (such as illite) from pore filling and subsequent redeposition downstream in pore throats of the fine siltstone component, otherwise dispersed in the original claystone structure. That could explain the relative decrease of the claystone and fine siltstone HU observations in Figure. II 4A. Simultaneously, the migration of fines from the detrital fragments within porous media could be seemingly the source of lesser representation of dispersed material and increased values of the saturated HU observations in Figure II. 5A.

Swelling clays, such as smectite and mixed-layer clays, first expand under favourable ionic conditions and then disintegrate and migrate. Smectites can be significantly affected by minor changes in temperature and water vapour pressure, leading to changes in rock strength, porosity, and permeability. the reactions of concern include (1) reversible collapse/expansion of the smectite layers due to loss/gain of interlayer water; (2) irreversible collapse due to loss of interlayer water and migration of interlayer cations into the 2:1 silicate layers; (3) irreversible reduction of the osmotic swelling ability through reaction in a steam atmosphere; and (4) inhomogeneous transformation of the smectite into an interstratified illite/smectite (Pusch & Karnland, 1996).

Accordingly, three scenarios could be proposed to interpret outliers in Figure II. 4B; non-swelling clays e.g., Kaolinites and illites, tend to detach from the rock surface, migrating (non-clay) fine particles e.g., cement, and smectite might swell and become free to move. These suggestions could explain the full or partial plugging of the pore throats and the increase of the minimum HU values outlier. Beyond that, collapsing of smectite, through one of the four above points, could lead to the adsorption of less water during the saturation phase, which together with particles releasing from

the detrital deposit structure could also create additional pore space. Appropriately, the maximum HU outlier in Figure II. 4B and Figure II.8 would result.

The exceptionally high coefficient of variation percentage of the detrital terrigenous fragments constituent (1039.39%) in Table II.1, reflects the high ratio of the standard deviation compared to the mean. The more extreme the outlier (32.33%), the more the standard deviation is affected, and the greater coefficient of variation arises. The large proportion of the minimum outlier probably results from migrating non-clay and/or non-swelling particles from pore walls during the flooding process. It could occur due to migration of smectite with the fluid flowing through the porous formation. In contrast, the fine siltstone coefficient of variation ratio is way lower than the detrital fragments variation (134.99%). This is relevant to the higher mean value (3.39%) and lower minimum porosity of outliers (15.14%). It could be said therefore that the lower the outlier ratio, the less the standard deviation is affected, and the smaller proportion of the variation coefficient produced. It is quite appropriate reliable to recall the throat plugging proposal here.

The low porosity outlier proportions of Claystone, carbonate, and albite seem not to affect the coefficient variation ratios. Relative high coefficients of variations have resulted from high standard deviation values comparable with low mean values. It is worthy to note that since these three last components are classified as filling material components or dispersible particles, the low minimum porosity outlier ratios are to be expected.

The descending porosity ratio of claystone accompanied by the lower carbonate porosity ratio over the three clusters in Figure II.10 seem to play a significant role in the porosity distribution of clusters. Comparing the claystone ratios across the three clusters; the no-porosity cluster has an extraordinary claystone proportion (around 23%), while the matrix and macro clusters show lower claystone ratios at 8.44% and 0.27%, respectively. Correspondingly, the carbonate cement has a high proportion in the no-porosity cluster (about 19%), and it decreases in both the matrix (1.66%) and macro- pore (0.27%) clusters. This observation suggests the higher the claystone and carbonate ratios, the lower the porosity proportions. It is also highly expected to find authigenic clay in the claystone component of the no-porosity cluster. Albite presence leads to pores becoming fully plugged in the no-porosity cluster (0.16%), whereas in the macro-pores cluster, albite is absent, and the detrital fragments occur instead (0.23%). It could be expected that pore spaces (macro-

pores) might be created within the portion of the detrital fragment because of the larger relative grain size.

Claystone and carbonate components are reasonably consistent; reducing claystone across the three clusters is associated with a decreasing carbonate ratio while albite would not produce a similar result. The difference of coincidence between these three components is related to the BCF diagenetic phases. The weathered residue of the basement mafic rocks accounts for authigenic deposits in the BCF playa basin. Albite cement (Pore-filling and interstitial) is formed by adding Na ions from an alkaline brine and evaporites to the Boda claystone sediments. The formation of albite was the reason for the depletion of Na ions in the claystone. Ca and K-enriched waters reacted with smectite and kaolinite to yield K-rich illite with precipitation of Ca in carbonate cement (Varga et al., 2005).

The Chi-square independence test emphasized that the clusters are related to their rock-type constituents at the 95% confidence level for a particular case. The Lambda and Pearson's R tests were applied to detect the association between clusters and rock-type variables. Based upon the Lambda value (0.0856), the reduction in error when a cluster is used to predict rock components is 8.56%. Also, Pearson's correlation shows a significant association between clusters and rock components at the 95% confidence level. The R-value was around 0.4.

The measurement protocol of the CT-laboratory allows a maximum of 10 HU absolute value noise. In the studied core, only 1.6% of the total number of voxels showed that the difference between the saturated and dry HUs was less than 10 HU. Table II. 3 shows the statistical characteristics of the density contrast between the dry and saturated scans and the calculated voxel porosity of this noisy-critical subset. The average mean of the difference between the saturated and dry HU values (<10 HU) was around 5. It can also be seen that the voxel porosity varies between 0.028 % and 0.40 % in this subset. The corresponding mean voxel-porosity is 0.17%. If we suppose that all HU contrast measured in this critical subgroup is noise, then the average voxel-porosity calculated for the whole core, 2.51%, can be decreased by a minimum of 0.028% porosity and a maximum of 0.40% porosity. So the average voxel porosity corrected by the expected noise may vary between 2.11% and 2.34%.

Table II. 3: Statistical characteristics of the density contrast between the dry and saturated scans and the calculated voxel porosity of the 10 HU absolute value noise.

	Valid N	Mean	Min.	Max.	Std.Dev
FLD-DRY (HU)	246187	5.501	1	10	2.869
Porosity (%)	246187	0.175	0.028	0.4	0.091

By neglecting the noise effect, the difference between the CT porosity scanned volume, and the mercury porosity means value in (Table II. 2) is caused due to the limitation of mercury measurements. Small pore volumes are usually not accessed by the mercury, even at the highest pressures. Unreachable minute pores in the Hg method reduce the porosity mean to 2.02%, while the mean porosity of the CT scans is 2.57%. However, the helium molecule's small size enables its entrance into the narrow pore structures and penetration into even the smallest pores. So, it gives a similar value for the porosity mean as the scanned CT volume (2.51%).

The hypothesis testing has been executed to determine which laboratory pore measurements should be considered and which should be discarded. The null hypothesis assumed that the difference between the mean CT and Hg porosity values are equal to zero. As a result, the null hypothesis is rejected at the 95% confidence level, and the confidence interval shows that the values of (CT mean= Hg mean) supported by data fall between (0.272 and 0.827). In the mean CT and He values comparison, the null hypothesis could not be rejected since the confidence interval supported by the data falls between (-0.217 and 0.337). From this perspective, only the He measurement could be considered reliable.

2.5. Summary

This work proposed a straightforward procedure to estimate the rocks' petrophysical properties of a selected core sample volume. The dual CT scans' parameters were analyzed to establish the direct relationship between the rock-forming components and the petrophysical properties. Voxel-porosity of the rock constituents was successfully classified into three major clusters based on porosity and textural patterns.

Two major pore regimes are demonstrated by the heterogeneous spatial distribution of pore volume; matrix porosity and macro- porosity. Micropores from the matrix cluster occupy a significant proportion of the total porosity. Authigenic minerals play an influential role in decreasing the pore volume and plugging the pore throats via the swelling and migration of fine particles. Obtained mean porosity value corresponds well with the mean porosity measured by helium porosimetry. The discrepancy between the mean CT porosity value and the mean porosity value obtained by Hg measurements can be assigned to the limitations of the laboratory method concerning the inaccessibility of small pores to mercury penetration.

Cementation and the authigenic clay content are considered to be the main pore volume-controlling factors of the BCF core sample. However, sedimentary structures, i.e., convolute structures, could also be a significant porosity-improving factor.

Chapter III:

Assessing the representative elementary volume of rock types by X-ray computed tomography (CT) – a simple approach to demonstrate the heterogeneity of the Boda Claystone Formation in Hungary

Saja M. Abutaha

The University of Szeged, Department of Geology and Paleontology; 6722, Szeged, Egyetem utca 2-6, Hungary.
Emails; sajaabutaha@geo.u-szeged.hu

János Geiger

The University of Szeged, Department of Geology and Paleontology; 6722, Szeged, Egyetem utca 2-6, Hungary.
Emails; matska@geo.u-szeged.hu

Sándor Gulyás

The University of Szeged, Department of Geology and Paleontology; 6722, Szeged, Egyetem utca 2-6, Hungary.
Emails; gulyas.sandor@geo.u-szeged.hu).

Ferenc Fedor

GEOCHEM Ltd, 55/1 Viola str., Kozármisleny, H-7761, Hungary.
Email; fedor.ferenc@geochem-ltd.eu

Geologos Journal
27, 3: 157–172 (2021)
DOI: 10.2478/logos-2021-0018

3. Chapter III: Assessing the representative elementary volume of rock types by X-ray computed tomography (CT) – a simple approach to demonstrate the heterogeneity of the Boda Claystone Formation in Hungary.

By Saja M. Abutaha, János Geiger, Sándor Gulyás, Ferenc Fedor

3.1. Introduction

The scale of observation is a fundamental aspect in modelling material behaviour or deriving its effective macroscale parameters from the constituent relations governed by the spatial distribution of its components. Any given sample (i.e., rock sample) can be considered homogeneous when the scale of observation is large enough to obtain constant parameters of concern (Russo & Jury, 1987; Webster, 2000). Various geological processes such as deposition, diagenesis, erosion and structural deformation that ultimately control the geometry of sedimentary deposits leads to heterogeneity in rock bodies (Brown et al., 2000). Accurate determination of rock heterogeneity is critical for a variety of industrial applications. For instance, it plays a key role in determining the reservoir's ability to recover oil and gas (Russo & Jury, 1987; Chang & Gao, 1995; Muhlhaus & Oka, 1996; Webster, 2000), carbon geostorage efficiency (Feyel & Chaboche, 2000; Peerlings & Fleck, 2001; Kouznetsova et al., 2001, 2002), contaminant mitigation and natural source zone depletion (Bear & Bachmat, 1990; Clausnitzer & Hopmans, 1999), water discharge and extraction rates (Brown et al., 2000; Baveye et al., 2002) or geothermal energy production feasibility (e.g., Al-Raoush & Willson, 2005). It is thus essential to understand rock heterogeneity in detail so as to make reliable predictions or process optimisation.

One of the methods for quantifying heterogeneity is to use the Representative Elementary Volume (REV) (Figure III. 1). The REV of a rock mass is defined as the smallest volume over which the studied parameter (in this case, density), yields a constant value (Long et al., 1982; Shapiro & Andersson, 1983; Blum et al., 2007). The present study aims to quantify and evaluate the minimum volume of a 2m core sample of the of Boda Claystone Formation, that can capture a representative quantity of its physical heterogeneity (i.e., density). Three major routes were followed to fulfil the above target: i) based on the dominant rock-forming components, rock types were detected as

consecutive thin layers; the average HU of rock constituents was calculated for each of these, ii) the ARIMA SPC technique was applied to compute REV values of layers defined, iii) Computed REV values were generalised using the Monte-Carlo simulation method.

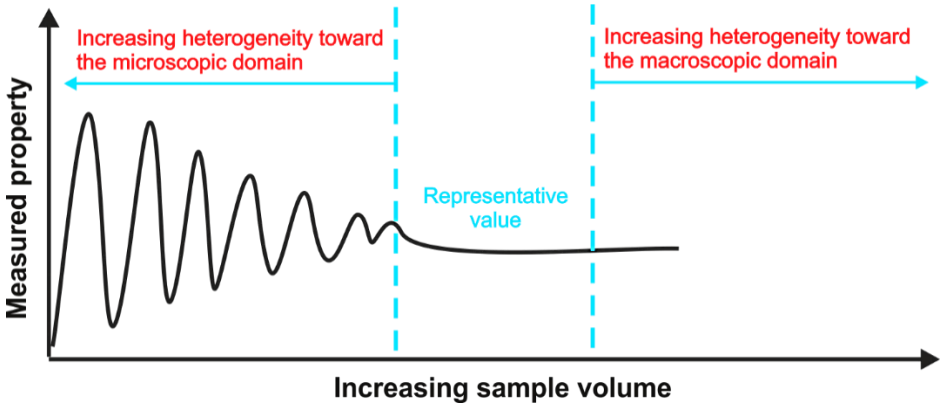

Figure III. 1: Definition of the Representative Elementary Volume, REV (after Bear, 1972).

3.2. Methodology

Figure III. 2 outlines the workflow applied to obtain the REV of the core sample studied.

3.2.1. Quantitative analysis of CT volume

As X-ray attenuation is dependent on density, voxel values can be used to make millimetre-scale measurements of bulk density in a non-destructive way. In the present paper, we use the term density or CT-density as a synonym of HU. Calculation of the relative percentages of the rock-forming components for each layer was a requisite of the vertical subdivision of the studied core volume (4L1, 4L2). After averaging the compositional data by layers, the dominant rock-forming component lent the name of the rock type to the corresponding layer (Figure III. 3; Table III. 1).

Linear correlation coefficients were calculated between any two pairs of rock-forming components averaged over a set of layers (Figure III. 2). In the depiction of the correlation structure, the cutoff value was $r^2=|0.7|$. That is, only those correlations where 50 per cent of the variance in a variable was predictable from the other one were regarded to be important relations.

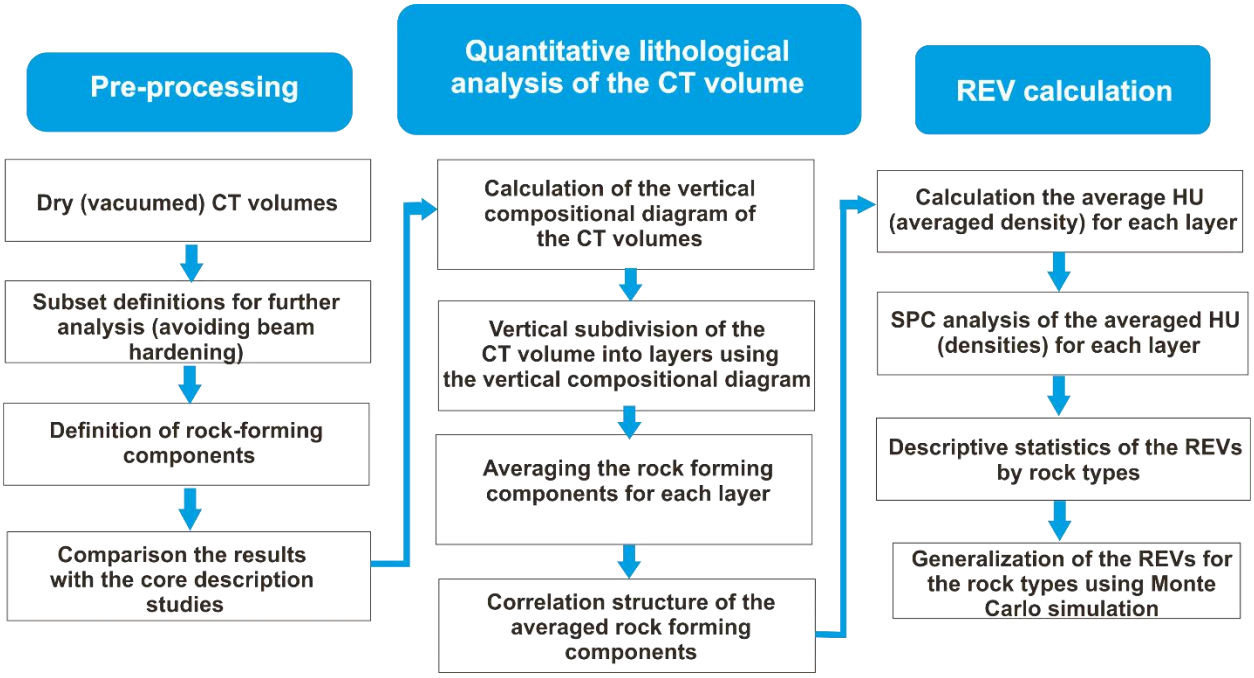

Figure III. 2: The workflow.

3.2.2. REV calculations

The REV for the layers chosen was performed by computing multiple incremental HU volumes in each layer. The process started with a cubic volume centred in the left-hand corner of the image. The volume was then expanded gradually by radial increments. The average of the acquired HU volumes were then computed and plotted on a chart of Statistical Process Control.

Statistical Process Control (SPC) is a family of methods to monitor and control a process using statistical methods (Shewhart, 1931; Montgomery, 1997; Oakland, 2003; Geiger, 2018). The objective was to detect anomalous values of the variable(s) analysed. In general, according to a certain tolerance margin and an objective value, two control limits, an upper control limit (UCL) and a lower control limit (LCL), are defined (Figure III. 4).

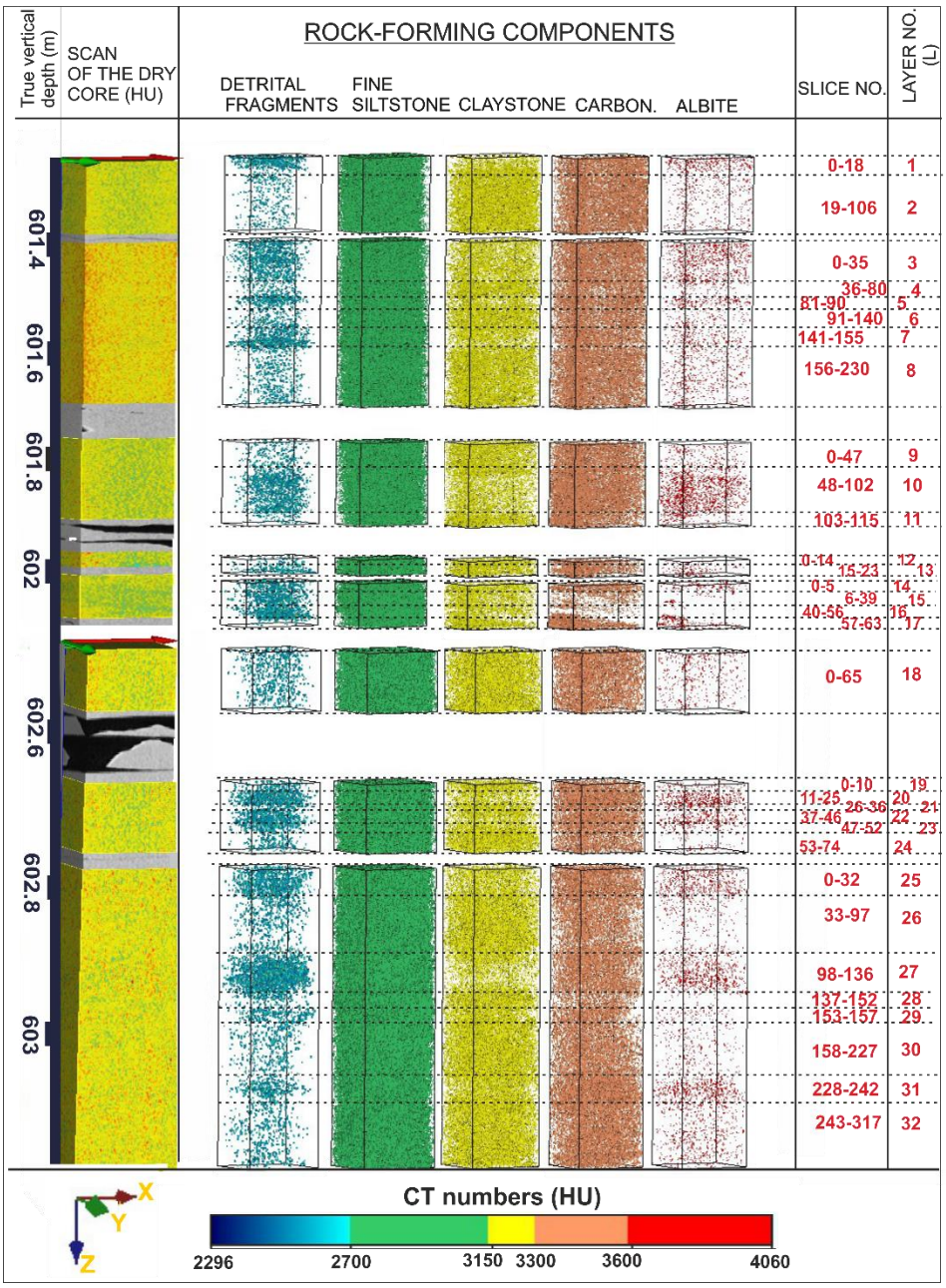

Figure III. 3: Rock-forming components and boundaries of layers defined.

Their practical definitions depend on the type of SPC applied. If the measurements are within the UCL and LCL, there is not a non-random pattern in the distribution, and the process is under

statistical control (Figure III. 4). However, if there are points (measurements) outside the limits, then for these points, the process is not controlled (Montgomery, 1997; Russo et al., 2012; Geiger, 2018).

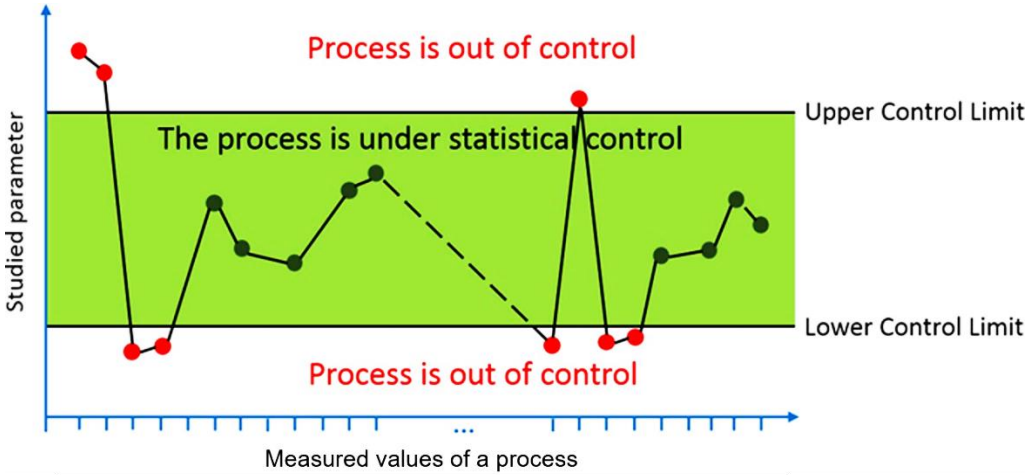

Figure III. 4: The SPC chart.

From the model describing the change of average HU in the gradually increasing voxel volumes the "objective value" was derived. The tolerance margins, UCL and LCL, were calculated from the variance of actual data around the model curve. In this way, the REV was the voxel volume number of realisations from which all HU values ended up being controlled (Figures III 4, 5D).

In general, the practice of SPC analysis consisted of three steps: understanding the process and specification limits, elimination of special sources of variations and monitoring the ongoing process (Polhemus 2005). In the present study, the last step is not used. Normally, SPC works under the assumption that the data observed are independent. However, in our case, a continuous transition violating independence between the different rock-forming components must be assumed. ARIMA (AutoRegressive Integrated Moving Average) charts are designed to handle suchsituations (e.g., Box et al., 1994; Polhemus, 2005; Russo et al., 2012). In their most general form, ARIMA (p, d, q) models consist of three characteristic terms: (1) a set of autoregressive terms (denoted by p), (2) a set of moving average terms or non-seasonal differences (denoted by

d), and (3) a set of lagged forecast errors in the prediction equation (denoted by q). The general form of the model is as follows (Polhemus, 2005):

$$Yt = \mu + \varphi_1 Y_{t-1} + \varphi_2 Y_{t-2} + \cdots + \varphi_p Y_{t-p} + a_t - \theta_1 a_{t-1} - \theta_2 a_{t-2} - \cdots - \theta_q a_{t-q} \qquad (1)$$

where μ is the constant, φ_k, is the autoregressive coefficient at lag k, θ_k, is the moving average coefficient at lag k, and a_{t-q} is the forecast error that was made at period $(t-k)$. The ARIMA charts procedure creates control charts for a single numeric variable where data have been collected either individually (this version was used here) or in subgroups. The out-of-control signals are based on the deviations of the process from this dynamic time series model (Figure III. 4). In this chart, the data are drawn around a centreline located at the expected value, μ, with control limits at

$$\mu \pm k \cdot \sigma^2 \qquad (2)$$

In the present study, $k = 1$. The mean and standard deviation depend on the ARIMA model specification (Polhemus, 2005). Figure III. 5 demonstrates a typical example of the applied analysis with ARIMA charts for the first layer shown in Figure 5. In Figure III. 5A, the components of the fitted ARIMA (1,0,0) model are shown. The explicit form of this model is a linear combination of a constant, one autoregressive term, and an error term (Figure III. 5B). The calculated centreline (average) and the UCL and LCL lines are shown in Figure III. 5C. Finally, in Figure III. 5D, the ARIMA chart can be seen, where the red dots indicate those parts of the series where severe deviations can be detected from the ARIMA (1,0,0) model (Figure III. 7C). From the 15th incremental step, a series of averaged HU values are within the envelopes (UCL and LCL). That is, the CT densities are fully controlled. Consequently, the REV can be identified as the volume behind the 15th incremental step (1.25 cm^3).

Calculations detailed above were performed for each of the 32 layers. A particular REV value obtained may depend on the volume of the corresponding layer, which makes the comparison complicated. To circumvent this problem the REV values were normalised by the corresponding layer volumes. In this way, the REV could be expressed as the volume percentage of the studied subvolume (layer). A Monte Carlo simulation uses repeated sampling to obtain the statistical properties of some phenomena. Gordon et al. (1993) published the first application of a Monte

Carlo resampling algorithm in Bayesian statistical inference: the bootstrap filter. The bootstrap algorithm did not require any assumption about the state-space or the noise of the system.

A

ARIMA(1,0,0) parameters

Parameter	Estimate	t-value	p-value
AR(1)	0.853	14.842	0.00
Mean	3149	136.306	0.00
Constant	463.50		

B

The ARIMA(1,0,0) model

$$Y_t = 463.502 + 0.853 \cdot Y_{t-1} + e_t$$

C

ARIMA chart parameters

$UCL = CL + 0.5\sigma^2$	**3158**
$Centerline\ (CL)$	3149
$LCL = CL - 0.5\sigma^2$	3140

D

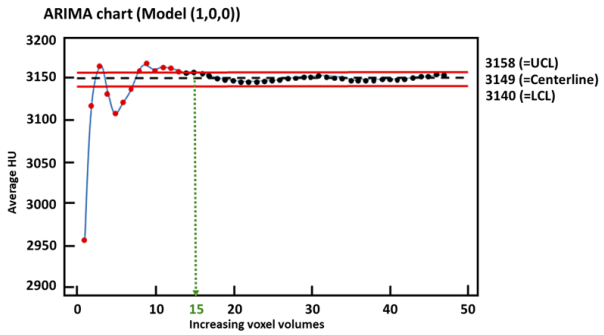

Figure III. 5: An example of the applied ARIMA charts. A – Parameters of the selected model; B – The explicit form of the selected model; C – Parameters of the ARIMA chart; D – ARIMA chart with the indication of the volume step where the REV can be defined.

The Monte Carlo simulation focuses on constantly repeating random samples to achieve certain results. Once the simulation is complete, the results are averaged to provide an estimate. We applied this approach to simulate 1,000 outcomes of the REV calculated for each rock type. By doing so, we assumed that those parts of the core studied fairly and representatively described the composition of the rock types of the entire core.

3.3. Results

3.3.1. Quantitative analyses of rock types

Based on the relative frequencies of compositional data, 32 thin layers (abbreviated as L) were defined throughout the 2-m core sample (Figure III. 5; Table III. 1). Each 3D brick of the dry scans

Table III. 1: Averaged compositional data by layers of the CT volumes

Layer NO.	Thickness (cm)	Averages of Rock-forming components %					Rock type	Sedimentary features
		Detrital fragment	Fine siltstone	Claystone	Carbonate	Albite		
L1	2.2	0.544	47.60	32.28	19.19	0.37	Clayey-siltstone	Dolomite intercalation, convolute bedding,
L2	10.8	0.048	41.53	39.76	16.61	0.04	Clayey-siltstone	
L3	4.375	0.301	45.62	33.94	19.79	0.32	Clayey-siltstone	
L4	5.5	0.145	47.60	35.59	16.51	0.14	Clayey-siltstone	
L5	1.125	0.530	48.21	32.04	18.89	0.32	Clayey-siltstone	
L6	6.125	0.147	47.89	35.98	15.89	0.08	Clayey-siltstone	Dolomite lenses and horizontal laminations
L7	1.750	0.81	53.60	30.3	15.05	0.14	Fine siltstone	Abundant albite nests on bedding surfaces
L8	9.250	0.07	44.94	37.82	17.08	0.07	Clayey-siltstone	
L9	5.875	0.08	43.77	38.02	18.02	0.10	Clayey-siltstone	Desiccation cracks, convolutions
L10	6.705	0.34	43.59	33.10	22.48	0.47	Clayey-siltstone	
L11	1.500	0.05	44.65	38.40	16.84	0.04	Clayey-siltstone	
L12	1.750	0.062	47.02	37.34	15.50	0.06	Clayey-siltstone	Abundant albite nests on bedding surfaces
L13	1.000	0.326	53.56	31.94	14.04	0.12	Fine siltstone	
L14	0.625	0.59	50.35	31.93	16.80	0.32	Fine siltstone	Albite nests and aleurolit intraclasts
L15	4.125	0.35	63.61	27.55	8.36	0.1	Fine siltstone	
L16	2.000	0.92	64.84	23.76	10.40	0.07	Fine siltstone	
L17	0.750	0.06	39.23	38.70	21.80	0.19	Clayey-siltstone	
L18	8.125	0.08	48.11	37.17	14.57	0.05	Clayey-siltstone	Albite nests & cracks
L19	1.250	0.12	48.64	36.14	15.01	0.07	Clayey-siltstone	
L20	1.750	0.5	48.26	31.28	19.53	0.41	Clayey-siltstone	Dominantly structureless,
L21	1.250	0.24	49.63	33.63	16.03	0.16	Clayey-siltstone	
L22	1.125	0.44	48.78	32.24	18.21	0.32	Clayey-siltstone	
L23	0.625	0.277	51.15	33.37	15.08	0.10	Fine siltstone	
L24	2.625	0.084	51.26	36.64	11.98	0.02	Fine siltstone	
L25	4.000	0.345	48.95	32.97	17.48	0.24	Clayey-siltstone	
L26	8.000	0.077	51.88	35.66	12.32	0.04	Fine siltstone	Crossbedding Synsedimentary fault,
L27	4.750	0.698	54.47	29.63	14.93	0.26	Fine siltstone	
L28	1.875	0.074	56.73	33.83	9.34	0.02	Fine siltstone	
L29	0.500	0.282	54.50	32.32	12.78	0.11	Fine siltstone	
L30	8.625	0.068	50.61	36.91	12.37	0.03	Fine siltstone	Crossbedding. Synsedimentary fault,
L31	1.750	0.192	44.04	35.05	20.41	0.29	Clayey-siltstone	Calcite precipitations in the cracks
L32	9.250	0.06	44.39	38.71	16.75	0.08	Clayey-siltstone	

included five rock constituents. They were (1) detrital fragments (HU <=2700), (2) fine siltstone (2700 HU-3150 HU), (3) claystone (3150 HU-3300 HU), (4) dolomite, and calcite cement (3300 HU-3600 HU), and (5) albite (HU>3600). Based on the most frequent rock-forming constituent we could classify the stacked slices of CT volumes into relatively thin consecutive layers.

The layer-averaged compositional frequencies showed the variability of the fine siltstone component to be very high (from 39% in layer L17 to 64.84% in layer L27), while that of claystone is significantly smaller (from 29.6% in layer L27 to 39% in layer L2). The average carbonate content may vary between 10% (in layer L28) and 22.5% (in layer L10). The abundance of albite and detrital fragment constituents is relatively low; their averages do not exceed 1%. Based on the dominant rock-forming constituent, two rock types could be defined: clayey siltstone and fine siltstone (Table III. 1). The dominant sedimentary structures of the clayey siltstone layers are convolute laminations, desiccation cracks with diagenetic calcite precipitations and dolomite lenses. The fine siltstone layers are characterized by cross-laminations with parallel set boundaries, with abundant albite nests appearing on the bedding surfaces, as well as synsedimentary faults (Table III. 1).

The linear correlation coefficients calculated between each pair of the rock-forming components show a feedback system among the fine siltstone, claystone and carbonate components. In the feedback, the higher the fine siltstone frequency, the smaller the claystone and carbonate content. The albite can linearly be related only to the carbonate content (Table III. 2).

Table III. 2: The linear (Pearson) correlation coefficients for averaged HU data of rock-forming components. Between brackets, the $p < 0.05$ values indicate statistically significant non-zero correlations at the 95.0% confidence level.

	Detrital fragments	**Fine siltstone**	**Claystone**	**Carbonate**	**Albite**
Detritalfragments	1	0.519 (p=0.002)	-0.878 (p=0)	-0.012 (p=0.947)	0.501 (p=0.004)
Fine siltstone		1	-0.785 (p=0)	-0.828 (p=0.303)	-0.253 (p=0.163)
Claystone			1	0.303 (p=0.091)	-0.352 (p=0.048)
Carbonate				1	0.705 (p=0)

3.3.2. REV calculations of CT density

As shown in Table III. 3, the REV values range from 0.7514 cm^3 up to 13.1072 cm^3. The data of Table III. 3 show that the largest REV values correspond to the presence of sedimentary structures (e.g., L9 and L11 in Table III. 3). Alternatively, such large REVs can be related to the highest (> 60%) siltstone constituent (e.g., L15 and L16 in Table III. 3). It can also be concluded that the average REV of the fine siltstone layers is larger than that of clayey siltstone layers. The former is 5.46 cm^3, the latter 4.57 cm^3 (Table III. 4, columns A and B).

Monte Carlo simulation with 1,000 runs was used to simulate the long-run properties of REV and the normalized REV for both lithologies. The results are summarised in Table III. 4 (columns C and D). In the studied core volume, the average REV of the CT density of clayey siltstone is slightly smaller (5.86 cm^3) than that of fine siltstone (6.54 cm^3). In the case of clayey siltstone, the normalized REV is 19.88% of the studied subvolume (on the scale of the studied core volume) on average, while this value is 22.84% for fine siltstone.

3.4. Discussion

Spatial variations in CT densities (HU) can be used to identify small-scale textural and structural heterogeneities in rocks. According to our findings, the calculated REV of CT-densities (HU values) can be directly related to the high textural heterogeneity caused by the sedimentary structures. Figure III. 6 shows four high-resolution CT images of convolute lamination (Figure III. 6A), a mud intraclast (Figure III. 6B), a crack (Figure III. 6C) and a pair of cross laminae (Figure III. 6D). The high and low-density components are very close to one another. The density contrast is high even within a short distance. In such situations, the series of the average CT densities of the increasing volumes show a monotonously increasing pattern until the volume does not cover the entire sedimentary structure. The normalized REV values are below 10% whenever the corresponding layer does not show any sedimentary structure (Table III. 3).

Table III. 3: Summary table of REV calculations.

Layer No.	The thickness of the layer (cm)	The volume of the layer (cm3)	REV (cm3)	Normalized REV (in the percent of the layer volume)	Rock type	Sedimentary structures
L1	2.25	22.48	1.3	5.78	Clayey-siltstone	
L2	10.88	108.64	4.7	4.33	Clayey-siltstone	
L3	4.38	43.71	2.1	4.80	Clayey-siltstone	
L4	5.50	54.95	2.1	3.82	Clayey-siltstone	
L5	1.13	11.24	3.0	26.69	Clayey-siltstone	
L6	6.13	61.19	10.7	17.49	Clayey-siltstone	Dolomite lenses and horizontal laminations
L7	1.75	17.48	1.1	6.29	Fine siltstone	Abundant albite nests on bedding surfaces
L8	9.25	92.41	2.8	3.03	Clayey-siltstone	
L9	5.88	58.69	11.2	19.08	Clayey-siltstone	Desiccation cracks, i, and convolutions
L10	6.75	67.43	11.2	16.61	Clayey-siltstone	
L11	1.50	14.99	11.1	74.07	Clayey-siltstone	
L12	1.75	17.48	0.7	4.00	Clayey-siltstone	Abundant albite nests on bedding surfaces
L13	1.00	9.99	1.3	13.01	Fine siltstone	
L14	0.63	6.24	1.6	25.63	Fine siltstone	Albite nests and aleurolit intraclasts
L15	4.13	41.21	10.7	25.97	Fine siltstone	
L16	2.00	19.98	12.6	63.06	Fine siltstone	
L17	0.75	7.49	2.2	29.36	Clayey-siltstone	
L18	8.13	81.17	13.1	16.14	Clayey-siltstone	Albite nests & cracks
L19	1.25	12.49	2.5	20.02	Clayey-siltstone	
L20	1.75	17.48	2.0	11.44	Clayey-siltstone	Dominantly structureless,
L21	1.25	12.49	2.6	20.82	Clayey-siltstone	
L22	1.13	11.24	2.0	17.80	Clayey-siltstone	
L23	0.63	6.24	1.4	22.42	Fine siltstone	
L24	2.63	26.22	1.5	5.72	Fine siltstone	
L25	4.00	39.96	2.2	5.51	Clayey-siltstone	
L26	8.00	79.92	11.8	14.76	Fine siltstone	Crossbedding Synsedimentary fault, with abundant albite nests
L27	4.75	47.45	9.5	20.02	Fine siltstone	
L28	1.88	18.73	1.1	5.87	Fine siltstone	
L29	0.50	5.00	1.1	21.93	Fine siltstone	
L30	8.63	86.16	11.8	13.74	Fine siltstone	Crossbedding Synsedimentary fault
L31	1.75	17.48	1.1	6.53	Clayey-siltstone	Calcite precipitations in the cracks
L32	9.25	92.41	2.7	2.94	Clayey-siltstone	

Our study was based on the statistical analysis of vacuumed CT scans. Consequently, in the validation of results, the effect of vacuuming on the integrity of core samples, specifically minerals (such as clay) that contain water as part of their crystal structure, must be considered. Various illite and illite/smectite-mixed assemblages constitute the dominant clay minerals of the Boda Claystone Formation (Németh & Máthé, 2016). Clay minerals are present as part of rock fragments, "allogenic clays" or authigenic clays (chapter 2). Partial to complete albitisation of detrital plagioclase of the BCF yielded Ca^{2+} to react with HCO^{3-} and Mg^{2+}($+Fe^{2+}$) to produce carbonate cement (Table III. 2; the positive relationship between albite and carbonate is ~0.7).

Bush & Jenkins (1975) reported that the drying process of core samples in an unhumidified oven will remove not only the free pore water but also the layers of non-liquid water from the clay minerals. They pointed out that, because this water is an integral part of the clays in the reservoir,

during laboratory drying will increase the available pore space and cause erroneously high porosity measurements. Different clay minerals exhibit different levels of sensitivity to drying, with smectite-type clays being the most sensitive and kaolinite the least (Keelan, 1982). The presence of smectite clay in narrow, slot-like flow channels, combined with its tendency to collapse when water is removed, may also cause large permeability (Soeder, 1986).

By comparing the highest and lowest ratios of the claystone rock-forming components layers in Table III. 1, we would obtain L9 and L16 layers. L9 has the highest claystone (38.02%) and smallest fine siltstone (43.77%) percentages, including desiccation crack and convolution, as deformation structures. In contrast, L16 shows the highest fine siltstone ratio (around 65%) and the lowest claystone percentage (23.76%) with a non-sedimentary structure realised. In layer L9, desiccation cracks are the dominant sedimentary structures. In this layer, the illite-smectite and smectite might be regarded as allogenic clay having been precipitated in mud cracks. Therefore, additive pore space resulting from clay shrinkage (during the drying process) might cause erroneously high porosity measurements, resulting in higher REV. In contrast, the clay in L16, which might be allogenic or/and authigenic and even be collapsed during the drying process, would not influence the inherent pore space ratio because of its low percentage. Studying the porosity distribution of the current BCF core sample in chapter 2, managed to confirm collapses of

smectite/illite structures during the drying/saturation process and postulated sedimentary structures, i.e., convolute structures, to act as significant porosity-improving factors.

Table III. 4: Summary statistics of actual and simulated REV values of clayey-siltstone and fine siltstone layers.

Summary statistics	A	B	C	D
	REV (cm^3)	Normalized REV (%)	Monte Carlo simulation of the REV (cm3) 1,000 runs	Monte Carlo simulation of the normalized REV (%) 1,000 runs
CLAYES SILTSTONE (N=20)				
Avg.	4.57	15.51	5.86	19.88
STD	4.18	16.11	4.57	17.76
Min	0.70	2.94	0.70	2.94
Max	13.10	74.07	13.10	74.07
FINE SILTSTONE (N=12)				
Avg.	5.46	19.87	6.54	22.84
STD	5.20	15.49	5.14	15.84
Min	1.10	5.72	1.10	5.72
Max	12.60	63.06	12.60	63.06

In other words: the presence of structures (sedimentary structures or even cracks) within the BCF core sample is more commonly interpreted as a type of heterogeneity, regardless of how regular their distribution is. The concept of increased heterogeneity could be viewed as a sharp density change in the CT number across a particular small section of a core (layer). Furthermore, internal void space in the layer's sedimentary features could be the real reason behind the high HU density contrast and the REV elevation. However, the core sample drying (vacuumed) process should be realised as an essential factor for creating pores and yielding illusory higher porosity measurements (clay collapsed). Those additive theoretical pores are presumed to have occurred in all layers with sedimentary structures (mud-cracks, cross-bedding, convolution) and cracks. Since the clayey-silt layers (L15, L16) show the maximum siltstone ratios (>60%), minimum claystone proportion, and

lack any sedimentary features, the high inherent porosity is expected to be accurate. The large REV defined can thus certainly be related to an actual pore heterogeneity.

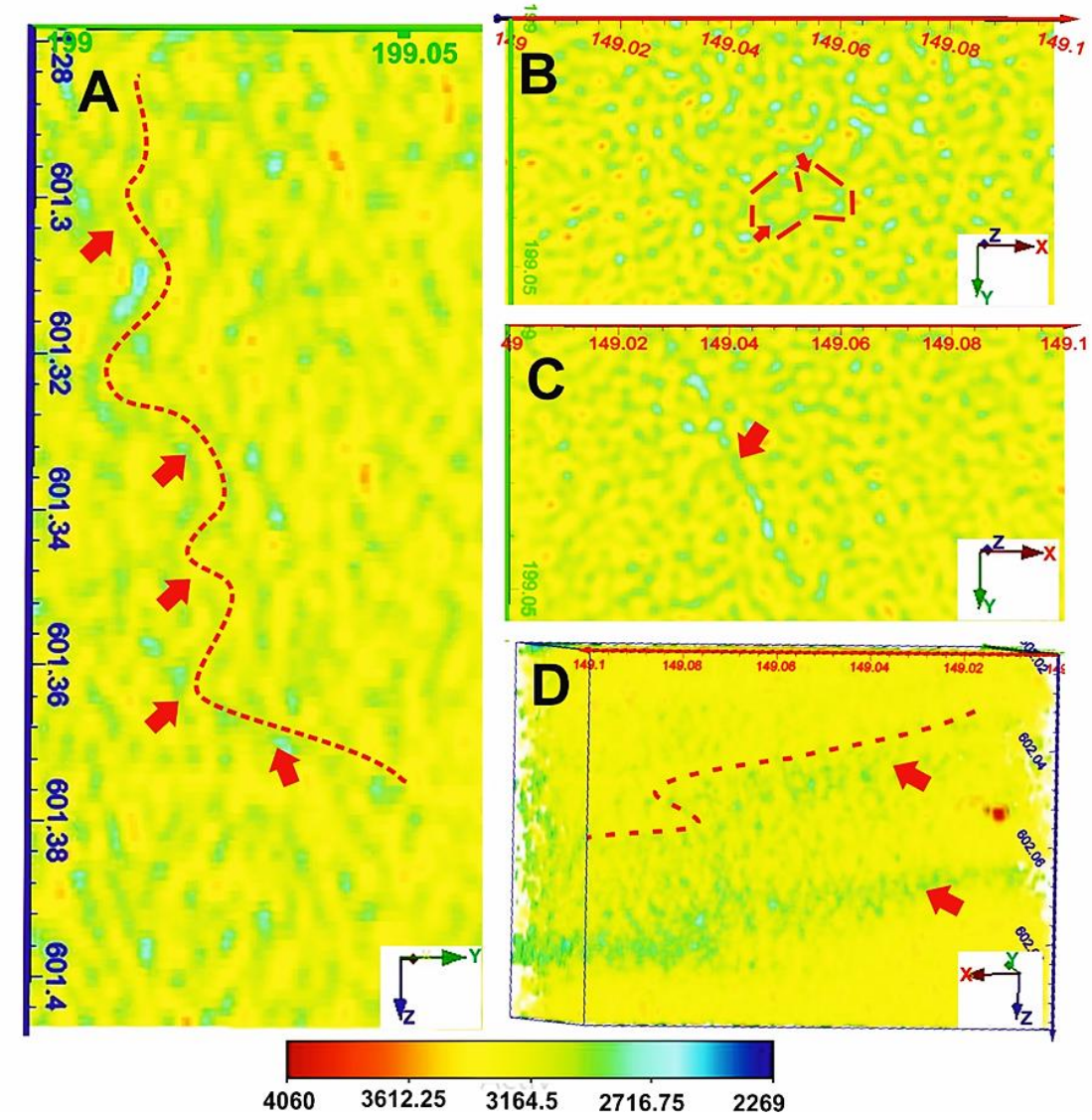

Figure III. 6: Sedimentary features of the defined layers. A – Convolute lamination; B – Mud intraclast; C – Crack; D – Cross-bedding. Red dashed lines show the sedimentary structure out-borders and red arrows point at actual deformation of detrital fragments - fine siltstone.

3.5. Conclusions

CT scanning is a powerful imaging technique for studying and analysing specimens in 3D without destroying them. CT numbers can also be used to proxy bulk density and identify sediment changes within a core sample. The present study aimed to quantify and evaluate the minimum volume of a Boda Claystone Formation core sample that could capture a representative quantity of physical heterogeneity (i.e., density) using the ARIMA SPC technique.

Stacked slices of CT volumes were grouped into relatively thin consecutive layers; thirty-two layers were defined. After averaging the compositional data by layers, the dominant rock-forming component provided the rock type name, i.e., fine siltstone layer (>50% siltstone component). Linear correlation coefficients between the averaged rock-forming components pairs were also studied across the set of layers.

The REV for the chosen layers was performed by computing multiple incremental HU volumes in each layer. The average CT densities of the increasing volumes showed a monotonously increasing pattern until the volume did not cover the entire sedimentary structure. The concept of increased heterogeneity, therefore, could be viewed as a sharp density change in the CT number (HU) across a particular small section of a core (layer). That is, the REV of CT densities can be directly related to the high textural heterogeneity caused by sedimentary structures, i.e., the largest REV values corresponded to the presence of sedimentary structure (e.g., L9 and L11), or such large REVs could be related to the largest (> 60%) siltstone constituent.

In general, the average REV of the fine siltstone layers was larger than that of clayey siltstone layers: 5.46 cm^3 and 4.57 cm^3, respectively. By normalising the REV values with the corresponding layer volumes, they could be expressed as volume percentage of the studied subvolume (layer).

The Monte Carlo simulation was used to simulate the long-run properties of REV and the normalised REV. As a result, the simulated REV (average) of the CT density of clayey siltstone was slightly smaller (5.86 cm^3) than that of fine siltstone (6.54 cm^3). Simulated percentages of the normalised REV values in clayey siltstone were 19.88% on average of the studied subvolume (on the scale of the studied core volume) and 22.84% for fine siltstone.

The presence of structures (sedimentary structures or cracks) within the BCF core sample is more commonly interpreted as a type of heterogeneity; the higher the heterogeneity, the higher REV. Seemingly, internal void space in the layers' sedimentary features might be the real reason for developing the high HU density contrast (increasing REV). We believe that the drying process of the core sample could essentially affect the available pore space and cause erroneous higher-porosity measurements (by collapsing clay), especially at sedimentary structures and cracks, where authigenic clay is expected to occur primarily.

Chapter IV:

Calculating the representative elementary volume of porosity using X-ray computed tomography: Boda Claystone Formation core sample/Hungary

Saja M. Abutaha

The University of Szeged, Department of Geology and Paleontology; 6722, Szeged, Egyetem utca 2-6, Hungary.
Emails; sajaabutaha@geo.u-szeged.hu

János Geiger

The University of Szeged, Department of Geology and Paleontology; 6722, Szeged, Egyetem utca 2-6, Hungary.
Emails; matska@geo.u-szeged.hu

Sándor Gulyás

The University of Szeged, Department of Geology and Paleontology; 6722, Szeged, Egyetem utca 2-6, Hungary.
Emails; gulyas.sandor@geo.u-szeged.hu).

Ferenc Fedor

GEOCHEM Ltd, 55/1 Viola str., Kozármisleny, H-7761, Hungary.
Email; fedor.ferenc@geochem-ltd.eu

Acta Geologica Slovaca (AGEOS) Journal
14, 1: 25–36 (2022)
Revised version accepted :2022-05-05

ISSN: 1338-0044; E-ISSN: 1338-5674

4. Chapter IV: Calculating the representative elementary volume of porosity using X-ray computed tomography: Boda Claystone Formation core sample/Hungary.

By Saja M. Abutaha, János Geiger, Sándor Gulyás, Ferenc Fedor

4.1. Introduction

Petrophysics is the study of the physical and chemical properties of rocks and their contained fluids (Tiab and Donaldson, 1996). Many petrophysical properties depend on the distribution of other properties such as mineralogy, pore size, or sedimentary. Accordingly, petrophysical properties can be fairly constant throughout a homogeneous reservoir or vary significantly from one location to another in an inhomogeneous or heterogeneous reservoir (Fitch et al., 2015). The scale of observation is a fundamental aspect in modeling material behavior or deriving its effective parameters from the constituent relations governed by the spatial distribution of its components. Frazer et al. (2005) commented that heterogeneity is an inherent, ubiquitous, and critical property that is strongly dependent on scales of observation and the methods of measurement used. Frazer et al. 2005 and Fitch et al., 2015 suggest that heterogeneity does not necessarily refer to the overall system, or individual rock/reservoir unit, but instead may be dealt with separately for individual units, properties, parameters, and measurement types. The issue of how the scale of measurement will be impacted by heterogeneity can be represented through the concept of a Representative Elementary Volume (REV) to characterize the point when increasing the size of a data population no longer impacts the average, or upscaled, the value obtained (Bear,1972; Bachmat and Bear, 1987).

In this chapter, CT scanning was applied in the study of a 5m long core of Boda Claystone Formation (BCF) to get an accurate insight into the variability of the porosity (Taud et al., 2005) and the density of the rock-forming components. The main objective of this study was to calculate the representative elementary volume (REV) of porosity.

Figure IV. 1A, shows the basic REV concept introduced by Bear (1972). This idea says that if an infinitesimal cubic elementary volume, at a point *P*, is considered, its porosity can take two values, 0 or 1. If the point *P* is inside a pore, the porosity at *P* is 1; otherwise, the porosity is 0. When we

increase the volume around *P* gradually, the corresponding porosities alternate between 0 and 1. This region is labeled as the 'Domain of microscopic' (Figure IV. 1A, left-hand side). Beyond a particular volume around *P* (V_{min}), the microscopic variations tend to decay, leaving only small-amplitude fluctuations due to the random distribution of pore sizes neighborhood of *P* (Figure IV. 1A, middle part). The homogenous region may become again heterogeneous after a particular volume (Figure IV. 1A, V_{max}). The region between V_{min} and V_{max} is called Representative Elementary Volume.

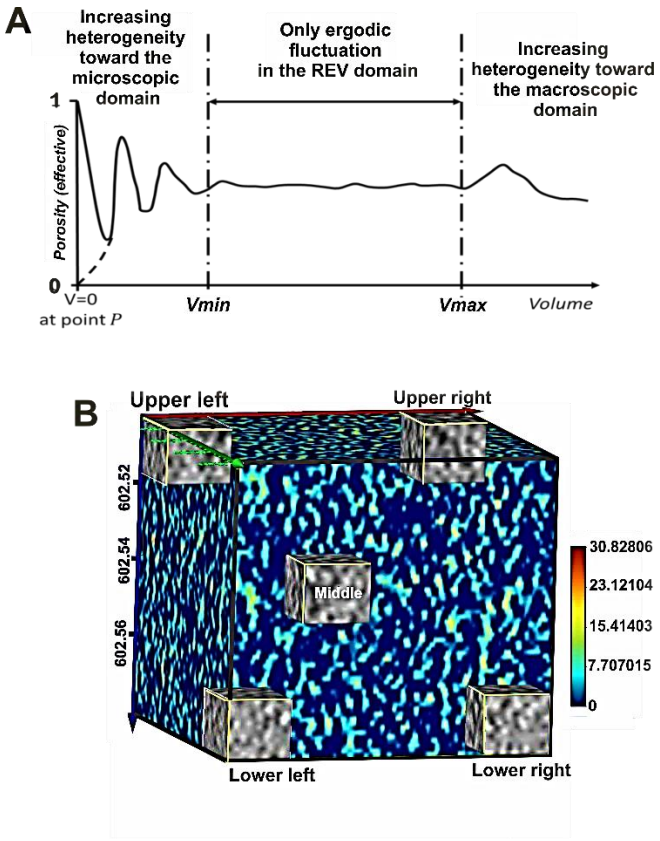

Figure IV.1: A: Definition of the Representative Elementary Volume, REV (after Bear, 1972). B: locations of initial cubic volume.

4.2. Methods

Figure IV. 2 shows the workflow followed to obtain the REV of voxel porosity.

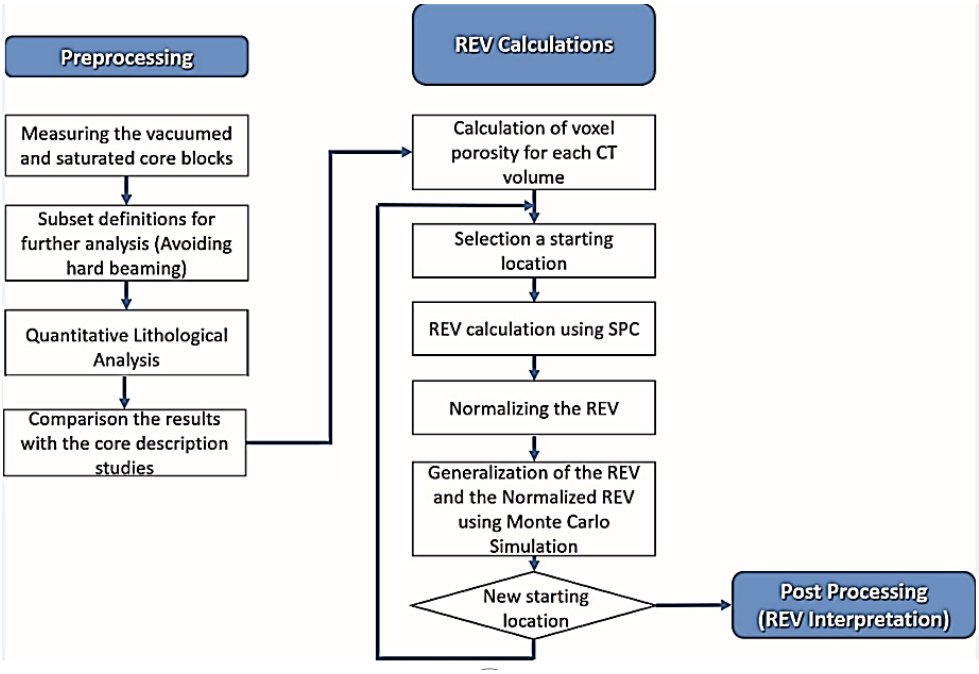

Figure IV. 2: The workflow

The pre-processing step was clarified in the methodology of chapter 3. The ARIMA SPC calculations (explained in chapter 3) were performed for each of the 20 CT volumes of the core sample of BCF (Table IV. 1). Since the REV value may depend on the size of the corresponding CT volume, we circumvent this problem by normalizing REVs with CT volumes (Table IV. 1). In this way, the REV could be expressed as the percentage of the studied volume.

The Monte Carlo simulation focuses on constantly repeating random samples to achieve certain results. Once the simulation is complete, the results are averaged to provide an estimate. Again, we applied this approach to simulate 1,000 outcomes of the REV calculated for each CT volume. By doing so, we assumed that those parts of the core studied fairly and representatively described the composition of the rock types of the entire core (Table IV. 2).

The prior procedure was five times iterated by varying the location of starting voxel volume; upper left, upper right, lower left, lower right, and middle. Table IV. 3 shows the means difference of REV- porosities of CT volumes.

In post-processing, when investigating the (REV), it is essential to fully understand the spatial distribution and variability of petrophysical properties of the core sample studied. In chapter 2,

we used a Boolean function to show the 3D spatial distributions of voxel-porosity by rock types. In that way, a straight connection between the rock-forming components and the voxel porosities would derive. In this chapter, the Boolean lattices were built up for 4L-1 and 4L-2 core volumes to visualize the three-dimensional distribution of voxel-porosities of rock-forming components. Then, relying on the methodology of chapter 3, layer boundaries of the 4L-1 and 4L-2 core volumes were defined. Finally, each layer's layer-averaged voxel-porosity frequencies were calculated to quantify the variability of pore distributions across different rock components.

Linear correlation coefficients were calculated between pairs of rock-forming components and corresponding average porosities over the CT layers.

The above post-processing steps were implemented to understand the reason for excluding the middle part of the core sample as an appropriate site for the initial volume of REV calculations.

4.3. Results and interpretations

4.3.1. Actual and simulated REV values

Detailed calculations of the REVs (cm^3) and the normalized REVs (%) of the twenty CT volumes of each location are summarized in Table IV 1. As of now, the term" location" is used to show the position of the initial volume of the REV calculation.

Table IV. 2 shows that the average REV values range from 16.56 cm^3 to 46.26 cm^3. The largest REV value corresponds to the upper left location, while the smallest REV relates to the upper right location (Table IV. 2).

The Normalized REVs, in the upper right and the middle locations, give almost equal volume percentages; ~9 %. They also have almost similar values at the lower right and lower left locations: 14% and 16% (on the scale of the studied core volume). However, the upper left location displays an extremely high average REV percentage, about 31% (Table IV. 2).

Monte Carlo simulation with 1,000 runs was used to simulate the long-run properties of REV and the normalized REV of voxel-porosity. The results are seen in Table IV. 2 (the last two columns). In the studied core volume, the average range of the simulated REV extends from 54 cm^3 to 65 cm^3. Notwithstanding, the middle location of the REV shows a much smaller value around 42 cm^3.

According to the simulation of the normalized REV values, the percentages on the scale of the studied core volume (from highest to smallest) are as follows: upper left location 40%, the lower right location 41.34%, and the lower-left location 23.86%, respectively. The upper right and the middle locations have almost the same percentage volumes, around 15.5%.

The average effective voxel-porosity of BCF is approximately 2.55%. In Table IV. 3, the REV porosities calculated from the sample's corners (upper left, upper right, lower left, and lower right) have mostly coincided with the general BCF average voxel-porosities of 2.46% - 2.58%. However, the middle location has an exceptionally larger REV porosity value (~2.8%).

The REV porosity of the middle position showed an odd high value (~2.8%). To understand this remarkable result, further quantifying analyses of porosity distribution was applied to the 2m bottom of the studied core sample (4L-1 and 4L-2 core volumes).

4.3.2. Quantitative analysis of porosity in 4L-1 and 4L-2 CT volumes

In Figure IV. 3, each 3D brick of the dry scan includes five-rock constituents: detrital fragments, fine siltstone, claystone, carbonate, and albite. The voxel porosity averages of these rock-forming components were calculated using dual CT scanning. The voxel porosities of the analyzed CT volumes are seen in the second column of Figure IV. 3. From the third to seventh columns, the porosity characters of the five rock-forming components are detailed. In the eighth column the porosities of the detrital fragments and the albite nests are pooled. The ninth column shows the small-scale layers defined by the dominant rock-forming component. Finally, the last column is for their average porosity.

Table IV. 1: Summary table of REV calculations.

Block No.	CT Volume No.	Voxel Volume of the CT brick (cm^3)	REV (cm^3)					Normalized REV (%) (REV (cm^3)/ CT brick volume)*100%				
			Upper left	Upper right	Lower left	Lower right	Middle	Upper left	Upper right	Lower left	Lower right	Middle
1L1	volume1	222.00	64.75	16.90	4.58	159.68	47.50	29.17	7.61	2.06	71.93	21.40
	volume2	236.00	74.08	10.62	36.85	26.57	24.00	31.39	4.50	15.61	11.26	10.17
	volume3	42.53	19.12	16.33	1.82	2.73	0.45	44.96	38.41	4.28	6.42	1.06
	volume4	85.05	19.05	13.23	10.56	17.72	31.19	22.40	15.55	12.41	20.83	36.67
	volume5	70.88	58.73	8.10	0.32	16.64	9.90	82.86	11.43	0.45	23.48	13.97
1L2	volume6	96.26	35.77	1.31	31.13	2.27	6.25	37.16	1.36	32.34	2.36	6.49
	volume7	313.88	95.33	16.90	13.94	17.90	1.97	30.37	5.38	4.44	5.70	0.63
	volume8	265.05	41.53	0.38	87.12	3.87	0.85	15.67	0.14	32.87	1.46	0.32
	volume9	101.84	41.53	10.62	2.08	0.42	1.35	40.78	10.43	2.04	0.41	1.33
2L1	volume10	439.92	64.75	41.97	55.12	9.24	0.12	14.72	9.54	12.53	2.10	0.03
	volume11	205.92	56.24	16.66	21.37	31.43	0.81	27.31	8.09	10.38	15.26	0.39
	volume12	198.43	41.53	1.26	13.09	16.65	0.81	20.93	0.64	6.60	8.39	0.41
4L1	volume13	126.00	7.87	1.30	50.50	51.52	0.12	6.25	1.03	40.08	40.88	0.09
	volume14	277.20	41.53	13.52	41.51	44.70	101.60	14.98	4.88	14.97	16.12	36.65
	volume15	136.42	20.26	8.17	10.25	26.90	3.62	14.85	5.99	7.51	19.72	2.65
	volume16	26.87	16.89	0.38	14.55	2.01	5.39	62.85	1.41	54.13	7.48	20.06
	volume17	74.40	36.83	8.17	40.99	1.49	0.12	49.50	10.97	55.10	2.00	0.16
4L2	volume18	92.16	7.87	0.16	2.96	6.50	6.25	8.54	0.17	3.21	7.06	6.78
	volume19	105.12	32.25	0.38	6.75	8.47	7.87	30.68	0.36	6.42	8.05	7.49
	volume20	442.08	149.30	144.88	15.68	22.24	107.94	33.77	32.77	3.55	5.03	24.42

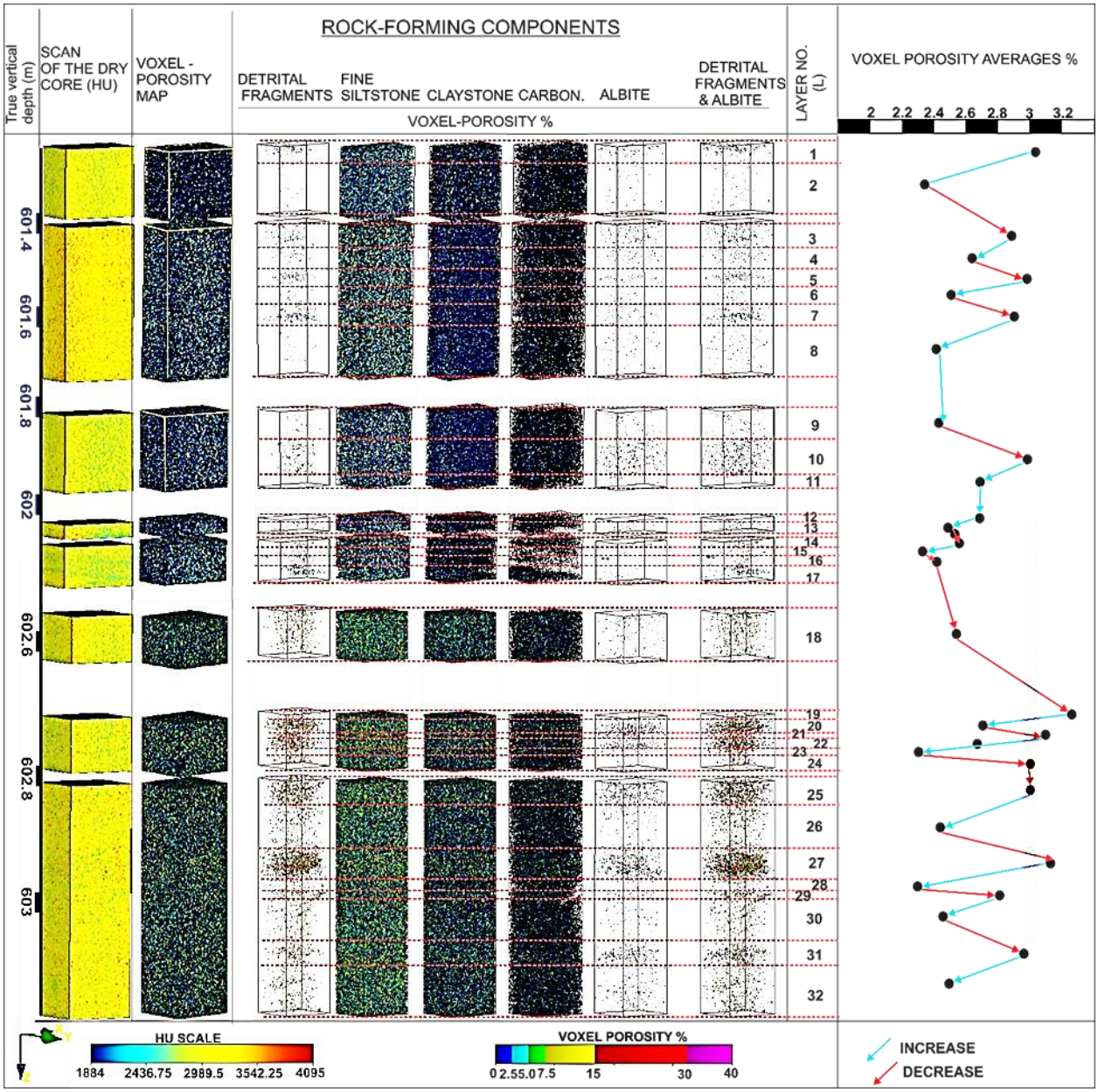

Figure IV. 3: Average porosity values of the five rock-forming components; boundaries of layers, and voxel-porosity averages of each layer were also defined

Table IV. 2: Summary statistics of actual and simulated REV values.

Starting point	Statistics characters	REV (cm^3)	Normalized REV (%)	Simulated REV at 1000 runs (cm^3)	Simulation of normalized REV at 1000 runs (%)
Upper left	Avg (cm^3)	46.26	30.96	64.80	39.65
	Md (cm^3)	41.53	29.77	60.53	37.98
	STD	33.39	18.79	30.56	15.47
	Min(cm^3)	7.87	6.25	7.45	8.70
	Max(cm^3)	149.30	82.26	149.75	78.19
Upper right	Avg (cm^3)	16.56	8.53	53.77	15.71
	Md (cm^3)	9.39	5.69	49.24	14.67
	STD	31.76	10.32	32.47	8.32
	Min(cm^3)	0.16	0.14	0.51	0.73
	Max(cm^3)	144.88	38.41	143.55	36.64
Lower right	Avg (cm^3)	23.45	13.80	61.44	41.34
	Md (cm^3)	16.45	7.77	55.68	40.11
	STD	35.16	16.84	34.96	17.96
	Min(cm^3)	0.42	0.41	1.44	2.83
	Max(cm^3)	159.83	71.93	158.02	87.31
Lower left	Avg (cm^3)	33.35	16.05	55.59	23.86
	Md (cm^3)	28.06	8.95	51.75	22.19
	STD	30.44	17.23	27.60	11.00
	Min(cm^3)	2.08	0.45	2.53	1.96
	Max(cm^3)	131.42	55.10	130.85	53.94
Middle	Avg (cm^3)	17.91	8.56	42.23	15.53
	Md (cm^3)	4.50	4.57	38.11	14.73
	STD	32.16	12.16	23.56	7.98
	Min(cm^3)	0.12	0.03	0.37	0.13
	Max(cm^3)	107.94	36.67	107.04	35.61

Table IV .3: Summary statistics of the mean porosities of the REVs.

	REVs porosity averages (%)				
	Upper left	**Upper right**	**Lower right**	**Lower left**	**Middle**
Average	2.52	2.58	2.55	2.47	2.78
Median	2.52	2.62	2.54	2.51	2.81
Standard deviation	0.21	0.22	0.22	0.185	0.26
Minimum	2.08	2.09	2.01	2.10	2.23
Maximum	2.88	2.92	2.88	2.85	3.05

Further, some virtual discernable relationships could be derived from Figure IV. 3. For instance, (1) The spatial distribution of the porosities of the detrital fragments and the albite

nests are very similar (the third and the seventh columns). (2) The higher the detrital fragments and albite amount, the larger the CT-layer-averaged porosity (the eighth and the tenth column). (3) The alternation of the CT layers with high and low layer-averaged porosity shows a cyclical pattern (the tenth column). To improve our understanding of these observations and be able to quantify them, it is important to invoke chapter 2 results of the voxel porosity regimes. In other words, under the umbrella of the pore volume clusters, re-define the relative frequencies of the average voxel porosities of the 32 layers by albite, and detrital fragments would be possible.

Chapter 2 classified the CT layers into three genetic groups based on data-mining techniques. The K-fold cross-validation algorithm was used to determine the cluster distribution number of the calculated voxel porosities (chapter 2). The first group was CT-layer with dominantly matrix porosity, where 75% of the voxel porosities were smaller than 7%. The second group was called CT-layers with dominantly macro-porosity. In this group, 75% of the voxel porosity ratios were larger than 7% and smaller than 19%. The larger than 19% voxel porosities were regarded as outliers and extremities. Finally, the third group was for no-porosity (pores~0).

Table IV. 4 shows two groups of small-scale layers. The first group (Table IV. 4, A) summarizes the relative frequencies of the tabulated averaged porosity values for layers containing a significant amount of detrital fragments and albite nests. Part B includes the same tabulation for layers that do not have a considerable amount of detrital fragments and albite nests. The cumulative percentages of the micro and matrix porosities are also calculated (Table IV. 4).

Layers with a significant amount of albite and detrital fragments (group A) show lower matrix porosity (82.68%), and higher percentages of the macro and the extremely large values of pores volume; 17.28% and 0.37%, respectively. In comparison, group B (where the albite and the detrital fragments are almost missed), illustrates a higher matrix porosity average (87.02%), and a lower larger pores volume; 12.89% for the macro porosity and less than 1% for the extremely large one. In view of this, we could suggest that the presence of both the detrital fragments and the albite constituents might increase the average porosity by enhancing the presence of the macro-porosity. Conversely, the absence of detrital fragments and albite might intensify the matrix-porosity. Matrix-pores can be related to the company of dense proportions of claystone- siltstone components. The linear correlation coefficients were calculated between the weight percentages of the rock-forming components and corresponding average porosities

(Figure IV. 4). It shows that the detrital fragments component has a moderate relationship with the 7-25% interval of the macroporosity; the r-value is around 0.55 (Figure IV. 4, upper black arrow). Whereas the albite has a significantly stronger linear relation to the macro-pores, the corresponding r-value is about 0.8 (Figure IV. 4, lower black arrow). That is, the pore spaces (macro-pores) might be created within the detrital fragments because of the larger relative grain size. The correlation structure of Figure IV. 4 can prove this theory. The high correlation coefficients of albite's weight percentage show that albite plays a substantial role in creating extra macro-pores. The negative correlation coefficient between the weight percentage of albite and the frequency of very small voxel porosities (Figure IV. 4, red arrow) can be explained by the process of CT measurement. Thus, during the saturation phase, the difference between the pore and injected water pressure may force some small movable particles to get out from some semi-filled pore space. In this way, the pore volume increases in the exhausted pores (Al-Yaseri et al., 2015; Hayatdavoudi & Ghalambor, 1996; Simon & Anderson, 1990; Zhou et al., 1995).

In our case, releasing albite particles from pore volume could generate an additive macro- pore space resulting from particles' migration. Those additive macro-pores might cause a higher macro-porosity measurement, resulting in a higher overall porosity ratio of each CT layer (Figure IV. 3, last column). However, if these small particles (i.e., albite) meet a narrow pore throat during their movement, they could cause throats to be plugged, by which the corresponding pore volume would

Table IV. 4: Tabulated relative frequencies of the average voxel porosities by layers.

A	**Layers**	**Matrix porosity**	**Macro-porosity**	**Extrem large values**
		(0-7)%	**(7-19)%**	**(20-25)%**
Layers with a significant amount of albite and detrital fragments	**L1**	82.08	17.87	0.44
	L3	83.35	16.62	0.29
	L5	82.40	17.56	0.37
	L7	83.26	16.70	0.30
	L10	82.81	17.16	0.36
	L20	81.22	18.69	0.55
	L22	82.38	17.58	0.39
	L25	82.73	17.24	0.33
	L27	81.65	18.28	0.52
	L29	84.15	15.79	0.19
	L31	83.37	16.60	0.30
	Average	***82.68***	***17.28***	***0.37***

B	**Layers without a significant amount of albite and detrital fragments**	**L2**	87.96	12.00	0.05
		L4	85.80	14.03	0.15
		L6	86.38	13.50	0.12
		L8	87.27	12.65	0.07
		L9	87.21	12.70	0.08
		L11	88.56	11.40	0.04
		L12	88.61	11.30	0.03
		L13	80.92	12.98	0.09
		L14	84.49	13.46	0.06
		L15	86.66	13.26	0.07
		L16	87.75	12.20	0.05
		L17	88.06	11.88	0.05
		L18	87.44	12.49	0.07
		L19	85.84	14.04	0.12
		L21	85.20	14.49	0.28
		L23	85.26	14.56	0.17
		L24	88.39	11.56	0.04
		L26	87.33	12.60	0.07
		L28	85.50	14.34	0.15
		L30	87.59	12.36	0.05
		L32	87.04	12.90	0.06
		Average	***87.02***	***12.89***	***0.09***

decrease (Ahmad et al., 2018). This process results in an erroneous negative correlation coefficient between the voxel porosity and the albite content. Figure IV. 5 clearly shows this situation.

Figure IV. 5 gives additional visual clues as to the presence of albite could be partly responsible for raising macro-porosity according to removing (migrating) the albite cement from pore volume (Figure IV. 5, red arrows), as well as reducing porosity by filling pores (Figure IV. 5, white arrows).

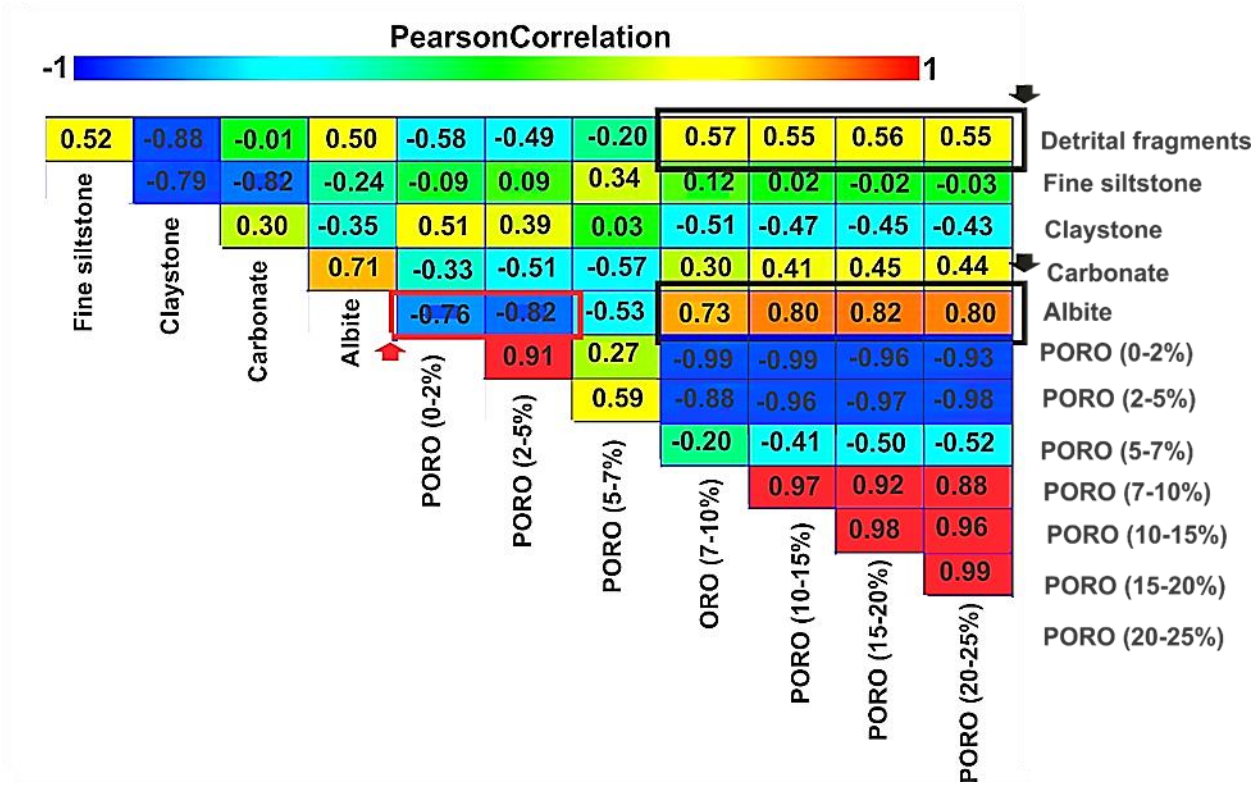

Figure IV. 4: The linear (Pearson) correlation coefficients for averaged porosity cut-off ratios and rock-forming components.

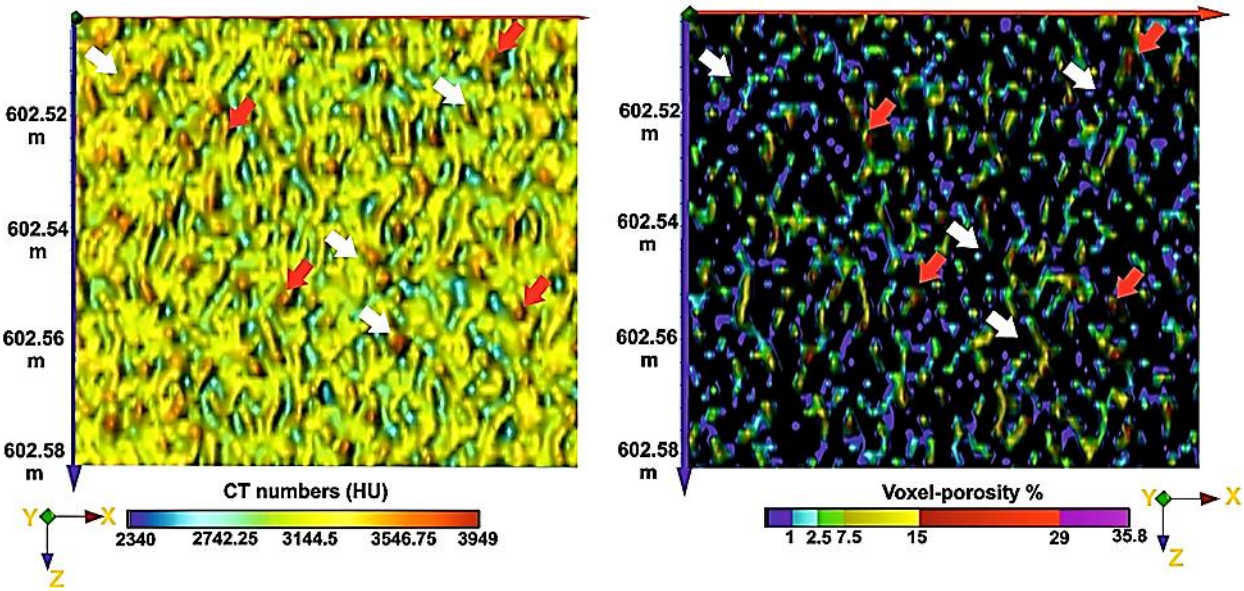

Figure IV. 5: Albite nests. On the left, the albite voxels appear with very high CT numbers. The corresponding voxel porosities are shown for the same slice on the right. The red arrows indicate albite removed from pore volumes, and white arrows point to the albite filled pores.

4.3.3. High porosity REV interpretation / why ought the core sample's middle part not stand for the inceptive volume of the REV calculations?

The frequent appearance of detrital fragments and albite intercalations reflects a repetitive pattern of porosity distributions in the middle part of the studied succession (Figure IV. 3). As the initial voxel volume started in such a medium (where albite and detrital fragments took place), the average porosity variations of the continuous volume transitions would become minimal at a high porosity REV value (~2.8%) because the intensive macro-pores exist. However, the scene was different when the initial voxel volume started from any four sample's corners (upper left, upper right, lower left, and lower right). The sample's core (center) was surrounded by a dense proportion of claystone-siltstone (mostly lacking albite and detrital fragments); matrix-porosity is highly expected (Figure IV. 3 /8th column). Therefore, since the continuous transition of the initial voxel volume occurred within the matrix porosity medium, the porosity REV value was significantly lower than that obtained from the middle. It was pretty close to the voxel porosity average of BCF (~2.5%). That is, the REV porosity value relies on the spatial position of the volume increasing process (initial volume).

4.4. Summary and conclusion

3D X-ray computed tomography images enabled obtaining accurate quantification of the variability of the porosity and the density of the rock-forming components. Such quantifications allowed performing REV analysis of porosity variations. CT scanning is applied in the current work's 5m core sample of Boda claystone formation (BCF). This study's main objective is to calculate the representative elementary volume (REV) of porosity. The REV calculation was carried out five times using the ARIMA SPC technique across the core sample. Each time it would start from a different cubic volume position. The obtained REVs were generalized using the Monte-Carlo simulation method, and the variations of REV porosity averages were thoroughly studied.

The average range of REV values was 16.56 cm^3 up to 46.26 cm^3. Monte Carlo simulation with 1,000 runs was used to simulate the long-run properties of REV and the normalized REV of voxel-porosity. The simulated REV range was 42 - 65 cm^3. Their volume percentages were; 15.5% and 40%, respectively. The REV porosity averages calculated from any sample's corners (upper left, upper right, lower left, and lower right) exhibited coincident approximations with

the general BCF average voxel-porosity; 2.47% - 2.58%. However, the middle site gave the oddity value, which was much higher than the rest of the Revs' porosity averages; it was around 2.8%.

The remarkable result associated with the highest REV porosity was studied deeply by applying further quantitative porosity analysis (post-processing steps). Accordingly, the following conclusions were derived: 1) both detrital fragments and albite constituents might influence the averaged porosity proportions of the studied layers by enhancing the presence of macro-porosity ratios (7-25%). Conversely, the absence of detrital fragments and albite might intensify the matrix-porosity ratios (0-7%). Matrix (throat)-pores are almost related to dense proportions of claystone- siltstone components. 2) although the detrital fragments might be a factor in the macro-pores presence, the albite almost plays a significant part in developing macro-porosity. 3) The saturation process of the core sample studied was the key to interpreting the dual role of the albite. Hence, the albite particles could release and re-deposited downstream in pore throats during the core sample saturation process. Compiling its particles might be causing throats to be plugged (decreasing porosity). Otherwise, releasing albite particles from pore volume might generate an extra macro-pore space (increasing porosity ratio).

As a result, when the initial voxels started from a medium where the macro-porosity is expected to exist primarily (detrital fragments and albite took place), the higher porosity REV was gained (~2.8%). Alternatively, when the volume of the initial voxel occurred within the matrix porosity medium (barely presence of albite and detrital fragments), the REV porosity ratio would be < 2.8%. That is to say, the middle part of the studied sample might not be adequate to be considered as an initial voxel volume of the REV calculation because its porosity REV value was significantly higher (~2.8%) than the average of the effective voxel- porosity of the BCF (~2.5%).

5. Chapter V: Thesis Summary

A core sample of BCF (Ib-4), about 5 m-long, was scanned at the Institute of Diagnostic Imaging and Radiation Oncology, University of Kaposvar, Hungary. X-ray computed tomography (CT) can reveal internal, three-dimensional details of objects in a non-destructive way and provide high-resolution, quantitative data in the form of CT numbers. The CT measurements were performed on a Siemens Emotion 6 medical scanner. The instrument operates at 120 kVp (peak kilovoltage), with 250 mAs (milliampere-seconds) current, and 1.0 s (sampling intervals). The lateral resolution was (0.1953 × 0.1953) mm^2 with 1.25 mm of scan-slice thickness. The image reconstruction matrix was 512 × 512 pixels. The field of view (FOV) was approximately 9.99 cm. CT images are stored in a DICOM (Digital and Imaging Communications in Medicine) format.

A 3D-nearest neighbor algorithm was used to build the 3D volumes of the scanned core blocks. This process resulted in two lattices, one for the vacuum dried and one for the saturated core volumes. The so-called scanning artifacts may obscure details of interest or cause the CT value of a single material to change in different parts of an image. The most commonly encountered artifact in CT scanning is beam hardening. Various methods have been developed to reduce or remove the effects of beam hardening. One of these is a subset of the CT volumes. It means removing the 3D image's outer edges; only central volumes are handled in quantitative analysis.

For the identification of rock-forming components of the core sample, CT HU intervals defined by PURAM for characteristic rock types of BCF were used as follows: detrital fragments (coarse siltstone): < 2700 HU, fine siltstone: 2700–3150 HU, claystone: 3150–3300 HU, calcite and/or dolomite: 3300–3600 HU, and albite: > 3600 HU. The reality of the rock-forming components was compared with macroscopic core descriptions. Calculating the relative percentages of the rock-forming components for scanned core parts was a prerequisite for defining small-scale layers (CT layers). The above information has been introduced in chapter1.

In the second chapter (1st article) we have quantified and evaluated the density and porosity characteristics of 1 m of the core sample (4L2) using medical CT. Each voxel of the 3D CT volume was described with three variables: dry CT number, saturated CT number, and effective

porosity. Disparity pore voxels were revealed using the genetic groups' algorithm of data-mining techniques. The K-fold cross-validation algorithm has been applied to determine the number of the most stable cluster. Moreover, the 3D spatial distributions of voxel-porosity by rock constituents and the 3D distribution of porosity clusters by rock components were found by Boolean function implementation.

As result; The terrigenous detrital fragments had the lowest porosity mean (0.16%) and the highest coefficient variation value (1039.39%). While the Fine siltstone component had the highest porosity mean (3.39%) and lower coefficient of variation (134.99%). The variation in coefficient proportions is related to the outlier ratios in each rock component. Independently of both the rock types and the sedimentary structures, three clusters could be defined: the micro-porosity, the macro-porosity, and no-porosity regimes. The microporosity showed a continuous 3D spatial appearance, while the macro porosity appeared in patches.

Since the three porosity clusters identified the 3D distributions of each rock-forming components, we could say in short, that the detrital fragments component almost dominates the macro porosity cluster. In comparison, the claystone prevails the matrix porosity cluster. However, Carbonate/ dolomite and albite constituents predominate the no-porosity cluster.

In closing, the micro-porosity regime could be related to high-density rock components, otherwise, the macro-porosity regime coupled with low density rock components. For example, the mean effective porosity of the matrix cluster is 3.39, whereas the average of the macropores regime is about 10.77, and zero for the no-porosity one. The ratios of voxel-porosity of the three clusters are; 30.37% for the matrix cluster, 14.65% for the macro-pores, and 55% the no-porosity cluster.

A hypothesis test has been applied to evaluate and compare the implemented CT pore measurements with conventional lab measurements, such as helium and mercury measurements. As a result, the He porosimetry measurements show quite close value for the calculated porosity mean of the CT scans image (2.51%), while the Hg measurement gives smaller porosity mean values (2.02%).

All things considered assert that the authigenic minerals play an influential role in decreasing the pore volume and plugging the pore throats via the swelling and migration of fine particles. Moreover, Cementation and the authigenic clay content are considered to be the main pore

volume-controlling factors of the BCF core sample. However, sedimentary structures, i.e., convolute structures, could also be a significant porosity-improving factor.

In the third chapter (2nd article), we confirmed the efficiency of using Representative Elementary Volume (REV) to quantify the inhomogeneity of CT densities of rock constituents of the Boda Claystone Formation. Thirty-two layers, 2 m core length (4L1, 4L2), were studied. Based on the dominant rock-forming constituent, two rock types would be defined, i.e., clayey siltstone (20 layers) and fine siltstone (12 layers). Eleven of these layers (clayey siltstone and fine siltstone) showed sedimentary features, such as, convolute laminations, desiccation cracks, cross-laminations, and cracks. The application of the Autoregressive Integrated Moving Averages, Statistical Process Control (ARIMA SPC) method to define Representative Elementary Volume (REV) of CT densities (Hounsfield unit values) affirmed the following results: 1) the highest REV values corresponded to the presence of sedimentary structures or high ratios of siltstone constituents (> 60%). 2) the REV average of the clayey siltstone was (5.86 cm^3) and (6.54 cm^3) of the fine siltstone. 3) normalized REV percentages of the clayey-siltstone and fine siltstone on the scale of the core volume studied were 19.88% and 22.84%, respectively. 4) whenever the corresponding layer did not reveal any sedimentary structure, the normalized REV values would be below 10%.

Ultimately, the internal void space in layers with sedimentary features might explain the salient textural heterogeneity and high REV values. The drying process of the core sample might also have played a significant role in increasing erroneous pore proportions by volume reduction of clay minerals, particularly within sedimentary structures, where authigenic clay and carbonate cement were presumed to be dominant.

In the fourth chapter (3rd article), The main objective was to calculate the representative elementary volume (REV) according to voxels' porosity. Physical properties of rock-forming components of a 5 m-long core sample of the Boda Claystone Formation (BCF) were acquired using 3D X-ray computed tomography images. The REV calculation was established using, again, the (ARIMA SPC) technique. This method (ARIMA SPC) was five times iterated by varying positions of starting voxel volume in the core sample: upper left, upper right, lower left, lower right, and middle. The average range of REV values was from 16.56 cm^3 to 46.26 cm^3. Monte Carlo simulation with 1,000 runs was used to simulate the long-run properties of REV and the normalized REV of voxel-porosity. The simulated REV values were 64.80 cm^3

in the upper left position, 61.44 cm^3 for the upper right, 55.59 cm^3 for the lower right, 53.77 cm^3 for the lower left, and 42.23 cm^3 for the middle.

According to the simulation of the normalized REVs, their volume percentages were as follows: 40 % for the upper left, 41.34 % in the lower right, and 23.86 % for the lower left. Lastly, the upper right and the central (middle) positions had almost the same percentage volumes, around 15.5 %. As the initial volume started from any core sample's corners, the porosity REV range would be between 2.47 % and 2.58 %, which is close to the average voxel porosity of BCF (2.55%). However, a deviant (higher) porosity REV value was attained from the center initiated volume (~ 2.8 %).

Eventually, we concluded that when the initial voxels started from a medium where the macro-porosity is expected to exist primarily (a considerable amount of detrital fragments and albite), the higher average porosity REV was gained (~2.8%). However, when the volume of the initial voxel occurred within the matrix porosity medium (barely presence of albite and detrital fragments), the average porosity REV would be < 2.8%. That is to say, the middle part of the studied sample might not be adequate to be considered as an initial voxel volume of the REV calculation.

6. Acknowledgment

We wish to acknowledge the Public Limited Company for Radioactive Waste Management (PURAM) for permitting the University of Szeged to use their data sets in scientific research work. This research has been sponsored by the Interdisciplinary Excellence Centre, Institute of Geography and Earth Sciences, Long Environmental Changes Research Team, Grants 20391-3/2018/ FEKUSTRAT and GINOP-2.3.2-15-2016- 00009 'ICER' of the European Union and the State of Hungary, Ministry of Human Capacities. Mecsekérc Ltd financed the measurements, while cofinancing came from the European Regional Development Fund.

7. References

Ahmad K.M., Kristály F. & Turzo Z., 2018: Effects of clay mineral and physico-chemical variables on sandstone rock permeability. Journal of Oil, Gas and Petrochemical Sciences, 18 – 26. doi:10.30881/jogps.00006

Akin, S. & Kovscek, A.R., 2003. Computed tomography in petroleum engineering research. [In:] Mees, F., Swennen, R., Van Geet, M. & Jacobs, P. (Eds): Application of X-ray computed tomography in the geosciences. Special Publication, Geological Society of London, 215, 23–38.

Al-Raoush R. & Papadopoulos A., 2010: Representative elementary volume analysis of porous media using X-ray computed tomography. Powder Technology. 200, 1 – 2, 69 – 77.

Al-Raoush, R. & Willson, C.S., 2005. Extraction of physically-representative pore network from unconsolidated porous media systems using synchrotron microtomography, Journal of Hydrology 23, 274–299.

Al-Yaseri A.Z., Lebedev M., Vogt S.J., Johns M.L., Barifcani A. & Iglauer S., 2015: Pore-scale analysis of formation damage in Bentheimer sandstone with in-situ NMR and micro-computed tomography experiments. J. Petrol. Sci., 129, 48 – 57. doi: 10.1016/j.petrol.2015.01.018.

Árkai P., Balogh K., Demény A., Fórizs I., Nagy G. & Máthé Z., 2000: Composition, diagenetic and post-diagenetic alterations of a possible radioactive waste repository site: The Boda Albitic Claystone Formation, southern Hungary. Acta Geologica Hungarica, 43, 351 – 378.

Arns, C. H., Knackstedt, M. A., Pinczewski, W. V. & Lindquist, W. B. 2001: Accurate estimation of transport properties from microtomographic images. -Geophysical Research Letters, 28, 3361–3364. doi: 10.1029/2001GL012987

Bachmat Y. & Bear J., 1987: On the concept and size of a representative elementary volume (Rev). In: Bear J. & Corapcioglu M.Y. (Eds.): Advances in Transport Phenomena in Porous Media, NATO ASI Series, 128, 3 – 20.

Balázs, G.Y.L., Lublóy, É. & Földes, T., 2018. Evaluation of concrete elements with X-Ray computed tomography. Journal of Materials in Civil Engineering 30, 1-9.

Balla z., 1987: Tectonics of the beukkian (north hungary) Mesozoic, relations to the West Carpathians, Dinarids. Acta Geol. Hung., 30(3–4), 257–287.

Barabás A. & Barabás-Stuhl Á., 1998: Stratigraphy of the Permian formations in the Mecsek Mountains and its surroundings. In: Stratigraphy of geological formations of Hungary. Geological and Geophysical Institute of Hungary, 187 – 215 p. (in Hungarian)

Barabás, A. & Barabás-Stuhl, Á., 1998. Stratigraphy of the Permian formations in the Mecsek Mountains and its surroundings. [In:] Stratigraphy of geological formations of Hungary. Geological and Geophysical Institute of Hungary, 187-215 (in Hungarian).

Baveye, P., Rogasik, H., Wendroth, O., Onasch, I. & Crawford, J.W., 2002. Effects of sampling volume on the measurement of soil physical properties: simulation with X-ray tomography data. Measurement Science and Technology, 13, 775–784.

Bear J., 1972: Dynamics of fluids in porous media. Dover Publications Inc., New York, 764 p.

Bear, J. & Bachmat, Y., 1990. Introduction to Modeling of Transport Phenomena in Porous Media. Kluwer Academic Press, Dordrecht, 575 pp.

Biswal B., Manwart C. & Hilfer R., 1998: Three-dimensional local porosity analysis of porous media. Physica A: Statistical Mechanics and its Applications, 255, 3 – 4, 221 – 241.

Blum, P., Mackay, R., Riley, M. & Knight, J., 2007. Performance assessment of a nuclear waste repository: upscaling coupled hydro-mechanical properties for far-field transport analysis. International Journal of Rock Mechanics and Mining Sciences 42, 781–792.

Boisson J.Y., 2005: Clay Club catalogue of characteristics of argillaceous rocks, Radioactive waste management, OECD Nuclear Energy Agency, 72 p. ISBN 92-64-01067-X

Bonner, B.P., Roberts, J.J. & Schneberk, D.J. 1994: Determining water content and distribution in reservoir graywacke from the northeast Geysers with X-ray computed tomography. -Geotherm. Resource Council Trans, 18, 305-310.

Borges J.A.R., Pires L.F., Cassaro F.A.M., Roque W.L., Heck R.J., Rosa J.A. & Wolf F.G., 2018: X-ray microtomography analysis of representative elementary volume (REV) of soil morphological and geometrical properties. Soil Tillage Research, 182, 112 – 122.

Box, G.E.P., Jenkins, G.M. & Reinsel, G.C., 1994. Time series analysis: Forecasting and control. 3rd Edition. Prentice Hall, Englewood Cliff, New Jersey, 619 pp.

Brown, G.O., Hsieh, H.T. & Lucero, D.A., 2000. Evaluation of laboratory dolomite core sample size using representative elementary volume concepts, Water Resources Research 36, 1199–1208.

Bush, D.C. & Jenkins, R.E., 1975. Proper Hydration of Clays for Rock Property Determinations. Journal of Petroleum Technology 22, 800-804.

Chang, C.S. & Gao, J., 1995. Second-gradient constitutive theory for granular material with random packing structure, International Journal of Solids and Structures, 32, 2279–2293.

Clausnitzer,V. & Hopmans J.W., 1999: Determination of phase-volume fractions from tomographic measurements in two-phase systems. Advances in Water Resources, 22, 577 – 584.

Cnudde, V., Masschaele, B., Dierick, M., Vlassenbroeck, J., Van Hoorebeke, L. & Jacobs, P. 2006: Recent progress in X-ray CT as a geosciences tool. -Applied Geochemistry, 21/5, 826–832. doi: 10.1016/j.apgeochem.2006.02.010

Coker, D. A., Torquato, S.& Dunsmuir, J. H. 1996: Morphology and physical properties of Fontainebleau sandstone via a tomographic analysis. -Journal of Geophysical Research, 101, 17497–17506. doi: 10.1029/96JB00811

Coles, M.E., Hazlett, R.D., Spanne, P., Soll, W.E., Muegge, E.L. & Jones, K.W. 1998: Pore level imaging of fluid transport using synchrotron X-ray microtomography. -Journal of Petroleum Science and Engineering,19/1–2, 55–63. doi: 10.1016/S0920-4105(97)00035-1

Coles, M.E., Hazlett, R.D., Spanne, P., Soll, W.E., Muegge, E.L. & Jones, K.W., 1998. Pore level imaging of fluid transport using synchrotron X-ray microtomography. Journal of Petroleum Science and Engineering 19, 55–63.

Coles, M.E., Muegge, E.L. & Sprunt, E.S. 1991: Applications of CAT scanning for oil and gas-production research. -IEEE Transactions on Nuclear Science, 38 /2, 510–515. doi: 10.1109/NSSMIC.1990.693464

Csicsák, J., 1999: The short-term program for the qualification of Boda Claystone Formation, Research final report, v. volume, hydrogeological, hydrochemical investigation program. Mecsekérc inc., Pécs [in hungarian].

Duchesne M.J., Moore F., Long B.F. & Labrie J., 2009: A rapid method for converting medical Computed Tomography scanner topogram attenuation scale to Hounsfield Unit scale and to obtain relative density values. Engineering Geology,103, 100 – 105.

Fazekas V., Majoros G.Y., Szederkényi T., 1987: Lower Permian volcanic sequences of Hungary. Acta Geol. Hung. 30(1–2), 21–34.

Fedor F., Máthé Z., Ács P. & Koroncz P., 2018: New results of Boda Claystone research - genesis, mineralogy, geochemistry, petrophysics. In: Norris S., Neeft E.A.C. & Van Geet M. (Eds.): Multiple

Roles of Clays in Radioactive Waste Confinement. Geological Society, London, Special Publications, 482 p., doi: 10.1144/SP482.13

Feyel, F. & Chaboche, J.-L., 2000. FE2 multiscale approach for modelling the elasto-viscoplastic behavior of long fiber SiC/Ti composite materials. Computer Methods in Applied Mechanics and Engineering 183, 309–330.

Fitch P, Lovell M., Davies S., Pritchard T. & Harvey P., 2015: An integrated and quantitative approach to petrophysical heterogeneity. Marine and Petroleum Geology, 63, 82 – 96.

Flannery, B.P., Deckman, H.W., Roberge, W.G. & D'amico, K.L. 1987: Three-dimensional X-ray microtomography. -Science, 237, 1439–1444. doi: 10.1126/science.237.4821.1439

Földes, T., 2011. Integrated processing based on CT measurement. Journal of Geometry and Physics 1, 23–41.

Földes, T., Kiss, B., Árgyelán, G., Bogner, P., Repa, I. & Hips, K., 2004. Application of medical computer tomography measurements in 3D reservoir characterization. Acta Geologica Hungarica, 47, 63–73.

Frazer G., Wulder M. & Niemann K., 2005: Simulation and quantification of the fine scale spatial pattern and heterogeneity of forest canopy structure: a lacunarity based method designed for analysis of continuous canopy heights. Forest Ecology and Management, 214, 65 – 90.

Fredrich, J. T., Greaves, R. H. & Martin, J. W. 1993: Pore geometry and transport properties of Fontainebleau sandstone. -International Journal of Rock Mechanics & Mining Sciences & Geomechanics Abstracts, 30, 691–697. doi: 10.1016/0148-9062(93)90007-Z

Garvey, C. J. & Hanlon, R. 2002: Computed tomography in clinical practice. -British Med. J., 324 /7345, 1077–1080. doi: 10.1136/bmj.324.7345.1077

Geiger, J., 2018. Statistical process control in the evaluation of geostatistical simulations. Central European Geology, 6/1, 50-72.

Gordon, N.J., Salmond, D.J. & Smith, A.F.M., 1993. Novel approach to nonlinear/non-Gaussian Bayesian state estimation, IEE Proceedings F (Radar and Signal Processing) 40, 107-113.

Guntoro, P.I., Ghorbani, Y., Koch, P. H.& Rosenkranz, J. 2019: X-ray Microcomputed Tomography (μCT) for Mineral Characterization; A Review of Data Analysis Methods. -Minerals, 9, 183p. doi: 10.3390/min9030183

Haas, J.& Péró, C.S. 2004: Mesozoic evolution of the Tisza Mega-unit. -International Journal of Earth Sciences, 93, 297–313

Haas, J.& Péró, C.S., 2004. Mesozoic evolution of the Tisza Mega-unit. International Journal of Earth Sciences 93, 297–313.

Hayatdavoudi A. & Ghalambor A., 1996: Controlling formation damage caused by kaolinite clay minerals: Part I. In: SPE Formation Damage Control Symposium, Society of Petroleum Engineers, SPE-31118-MS. doi: 10.2118/31118- MS.

Heismann B.J., Leppert J. & Stierstorfer K., 2003: Density and atomic number measurements with spectral x-ray attenuation method. Journal of Applied Physics, 94, 2073 – 2079.

Horváth F., 1993: Towards a mechanical model for the formations of the Pannonian basin. Tectonophysics, 226, 333–357.

Hounsfield, G.N., 1973. Computerized transverse axial scanning (tomography). 1. Description of system. British Journal of Radiology 46, 1016-1022.

Hove, A.O., Nilsen, V. & Leknes. J. 1988: Visualization of Xanthan Flood Behavior in Core Samples by Means of X-Ray Tomography.– SPEJDOE, 17342.

Jámbor, Á., 1964. A Mecsek hegység alsópermi képződményei [The Early Permian formations of the Mecsek Mts.]. Mecsekérc Ltd. Archives, Pécs, 127 pp.

Jones, K.W., Spanne, P., Webb, S.W., Conner, W.C., Beyerlein. R.A., Reagan. W. J. & Dautzenberg, F.M. 1991: Catalyst Analysis using Synchrotron X-ray Microscopy. -Nuc. Inst. Meth. Phy. Res., 56-57, 427-432. doi: 10.1016/0168-583X(91)96063-Q

Keelan, D.K., 1982. Core analysis for aid in reservoir description. Journal of Petroleum Technology 34, 2483-2489.

Ketcham, R.A. & Carlson, W.D., 2001. Acquisition, optimization and interpretation of X-ray computed tomographic imagery: applications to geosciences. Computational Geosciences 27, 381–400.

Konrád, G. 1999: The Boda Claystone Formation. The Geology of today for tomorrow. -Excursion Guide Book (A satellite conference of the World Conference of Science, Budapest), 65–75.

Konrád, G.Y., Sebe, K., Halász, A. & Babinszki, E., 2010. Sedimentology of a Permian playa lake: The Boda Claystone Formation, Hungary. Geologos 16, 27–41.

Kouznetsova, V., Brekelmans, W.A.M. & Baaijens, F.P.T., 2001. An approach to micro–macro modelling of heterogeneous materials. Computational Mechanics 27, 37–48.

Kouznetsova, V., Geers, M.G.D. & Brekelmans, W.A.M., 2002. Multi-scale constitutive modelling of heterogeneous materials with a gradient-enhanced computational scheme. International Journal for Numerical Methods in Engineering 54, 1235–1260.

Kovács, L.1999 a: Digest on the results of the short- term characterization programme of the Boda Claystone Formation. PURAM, Mecsekérc.

Lázár, K. &Máthé, Z. 2012: Claystone as a potetial host rock for nuclear waste storage. in: Valaškova, m. & Martynkova, G.S. (eds) 'Clay minerals in nature – their characterization, modification and application'. Intechopen, London, 55–80.

Ledley, R..S., Chiro, G.D., Luessenhop, A.J. & Twigg, H.L. 1974: Computerized transaxial X-ray tomography of the human body. -Science, 186, 207-212.

Long, J., Remer, J., Wilson, C. & Witherspoon, P., 1982. Porous media equivalents for networks of discontinuous fractures. Water Resources Research 18, 645–658.

Lontocroy, M., Dutilleul, P., Prasher, S. O., Han, L. W. & Smith, D. L. 2005: Computed tomography scanning for three-dimensional imaging and complexity analysis of developing root systems. -Canadian Journal of Botany, 83, 1434–1442. doi: 10.1139/b05-118

Louis, L., Wong, T. F. & Baud, P. 2007: Imaging strain localization by X-ray radiography and digital image correlation: deformation bands in Rothbach sandstone. -Journal of Structural Geology, 29 /1, 129–140. doi: 10.1016/j.jsg.2006.07.015

Máthé Z., 2015: Results of mineralogical, petrological and geochemical investigation of Boda Claystone Formation. PhD thesis summary, ELTE Department of Petrology and Geology, Budapest, 1-6p. [in Hungarian]

Máthé, Z. & Varga, A., 2012. "Ízesíto" a permi Bodai Agyagko Formáció oskörnyezeti rekonstrukciójához: kosó utáni pszeudomorfózák a BAT-4 fúrás agyagkomintáiban. ["Seasoning" to the palaeoenvironmental reconstruction of the Permian Boda Claystone Formation: pseudomorphs after halite in the claystone samples of the deep drillings BAT-4]. Földtani Közlöny 142, 201-204 (in Hungarian with English summary).

Máthé, Z., 1998. Summary report of the site characterization program of the Boda Siltstone Formation. Mecsek Ore Environment Company, Pécs, 4.

McCann, T. 2008: The geology of central europe vol. 1 Precambrian and Palaeozoic. — Geological Society, London. 748.

Mév 1993: report about the results of geological research related to the recommended mecsek deep waste disposal site in 1989–1992. Hungarian research report. (Mév, Pécs). Mév database.

Montgomery D.C., 1997: Introduction to Statistical Quality Control. John Wiley and Sons, New York, 759 p.

Moss R.M., Pepin G.P. & Davis L.A. 1990: Direct measurement of the constituent porosities in a dual porosity matrix. SCA conference, 9003.

Muhlhaus, H.B. & Oka, F., 1996. Dispersion and wave propagation in discrete and continuous models for granular materials. International Journal of Solids and Structures 33, 271–283.

Nahmani, J., Capowiez, Y. & Lavelle, P. 2005: Effects of metal pollution on soil macroinvertebrate burrow systems. -Biology and Fertility of Soils, 42, 31–39. doi: 10.1007/s00374-005-0865-4

Németh, T. & Máthé, Z., 2016. Clay mineralogy of the Boda Claystone Formation (Mecsek Mts., SW Hungary). Open Geoscience 8, 259–274.

Nichols, M.C., Kinney, J. H., Johnson, Q.C., Saroyan, R.A., Bonse, U., Nusshardt. R. & Pahl. R. 1989: Synchrotron Microtomography of Supported Catalysts. -Rev. Sci. Inst., 60/7, 2475. doi: 10.1063/1.1140703

Oakland, J.S., 2003. Statistical process control. Butterworth-Heineman, Oxford, 460 pp.

Peerlings, R.H.J. & Fleck, N.A., 2001. Numerical analysis of strain gradient effects in periodic media. Journal De Physique IV, 11, 153–160.

Polhemus, N.W., 2005. How to: Construct a control chart for autocorrelated data. StatPoint Technologies, Herndon, 16 pp.

Purcell, C., Harbert, W., Soong, Y., Mclendon, T.R., Haljasmaa, I.V., Mcintyre, D.& Jikich, J. 2009: Velocity measurements in reservoir rock samples from the SACROC unit using various pore fluids, and integration into a seismic survey taken before and after a CO2 sequestration flood. -In: Gale, J., Herzog, H., Braitsch, J. (Eds.), Energy Procedia.: Greenhouse Gas Control Technologies, 9. Elsevier Science, Amsterdam, 2323–2331. doi: 10.1016/j.egypro.2009.01.302

Pusch, R., & Karnland, O. 1996: Physico/chemical stability of smectite clays. -Engineering Geology,41/1-4, 73-85. Doi: 10.1016/0013-7952(95)00027-5.

Pyraknolte, L.J., Montemagno, C.D. & Nolte, D.D. 1997: Volumetric imaging of aperture distributions in connected fracture networks. -Geophysical Research Letters, 24 /18, 2343–2346.

Remmy, R.R. & Ferrell, R.E. 1989: Distribution and origin of analcime in marginal lacustrine mudstones of the Green River Formation, south-central Uinta Basin, Utah. Clays and Clay Minerals, 37, 419–432.

Russo, D. & Jury, W.A., 1987. A theoretical study of the estimation of the correlation scale in spatially varied fields, 2. Nonstationary fields. Water Resources Research 23, 1269–1279.

Russo, S.L., Camargo, M.E. & Fabris, J.P., 2012. Applications of control charts ARIMA for autocorrelated data. [In:] Nezhad, M.S.F. (Ed.): Practical Concepts of Quality Control. InTech, Rijeka, 31–53.

Schneider, J., Körner, F., Roscher, M. & Kroner, U., 2006. Permian climate development in the northern peri-Tethys area – the Lodève basin, French Massif Central, compared in a European and global context. Palaeogeography, Palaeoclimatology, Palaeoecology 240, 161–183.

Schwartz, M. F., Saffran, E. M., Fink, R. B., Myers, J. L. & Martin, N. 1994: Mapping therapy: A treatment programme for agrammatism. -Aphasiology, 8/1, 19–54. doi: 10.1080/02687039408248639.

Shapiro, A.M. & Andersson, J., 1983. Steady state fluid response in fractured rock: a boundary element solution for a coupled, discrete fracture continuum model. Water Resources Research 19, 959–969.

Shewhart, W.A., 1931. Economic control of quality of the manufactured product. Van Nostrand, New York, 501 pp.

Simon D. & Anderson M., 1990: Stability of clay minerals in acid. In: SPE Formation Damage Control Symposium. Society of Petroleum Engineers, SPE-19422- MS, doi: 10.2118/19422-MS.

Soeder, D.J., 1986. Laboratory drying procedures and the permeability of tight sandstone core. SPE Formation Evaluation 1, 16-22.

Spanne, P. & Rivers, M. 1987: Computerized Microtomography using Synchrotron Radiation from the NSLS. -Nucl. Instr. Meth. Phy. Res., 24-25, 1063, 67p. doi: 10.1016/S0168-583X(87)80312-9

Sprunt, E.S., Desai, K.P., Coles, M.E., Davis. R.M. & Muegge, E.L. 1991: Cat Scan Monitored Electrical Resistivity Measurements Show Problems Achieving Homogeneous Saturation. -Soc Pet. Eng., 21433.

Sutton, S. R., Bertsch, P. M., Newville, M., Rivers, M., Lanzirotti, A. & Eng, P. 2002: Microfluorescence and microtomography analyses of heterogeneous earth and environmental materials. -In: FENTER, P., RIVERS, M., STURCHIO, N. & SUTTON, S. (eds), Applications of Synchrotron Radiation in Low-Temperature Geochemistry and Environmental Sciences. Reviews in Mineralogy and Geochemistry, 49, 429–483. Doi: 10.1515/9781501508882-014

Szkfi 1990: Determination of the permeability of Lower Permian BCF samples by constant reservoir pressure at changing pore pressure and temperature, Hungarian hydrocarbon institute report, nagykanizsa [inhungarian].

Szkfi 1991: Determination of the permeability of Lower Permian BCF samples by constant reservoir pressure at changing pore pressure and temperature, Hungarian hydrocarbon institute, part of report, nagykanizsa, 1991 [in hungarian].

Taud, H., Martinez-Angeles, T.R., Parrot, J.F. & Hernandez-Escobedo, L., 2005. Porosity estimation method by X-ray computed tomography. Journal of Petroleum Science and Engineering 47, 209 – 217.

Tiab D. & Donaldson E., 1996: Petrophysics: Theory and Practice of Measuring Reservoir Rock and Fluid Properties. Gulf Publishing Company, Houston. 706 p.

Van Geet, M., Swennen, R. & Wevers, M., 2000. Quantitative analysis of reservoir rocks by microfocus X-ray computerised tomography. Sedimentary Geology 132, 25–36.

Van kaick, G. & Delorme, S. 2005: Computed tomography in various fields outside medicine. -European Radiology, 15/S4, D74–D81. 10.1007/s10406-005-013

Varga A., Raucsik B., Szakmány G.Y. & Máthé Z., 2006: Mineralogical, petrological and geochemical characteristics of the siliciclastic rock types of Boda Siltstone Formation. Bulletin of the Hungarian Geological Society, 136, 2, 201 – 232

Varga A.R., Szakmány G.Y., Raucsik B. & Máthé Z., 2005: Chemical composition, provenance and early diagenetic processes of playa lake deposits from the Boda Siltstone Formation (Upper Permian), SW Hungary. Acta Geologica Hungarica, 48, 49 – 68.

Verhelst, F., Vervoort, A., De bosscher, P.H. & Marchal, G. 1995: X-ray computerized tomography: determination of heterogeneities in rock samples. -In: Proc. 8th Int. Congress of Rock Mechanics. ISRM/Balkema, 1,105-108.

Vinegar, H.J. & Wellington, S.L. 1987: Tomographic imaging of three-phase flow experiments. -The Review of Scientific Instruments, 58 /1, 96–107. doi: 10.1063/1.1139522

Vozárová, A., Ebner, F., Kovács, S., Kräutner, H-G., Szederkényi, T., Kristić, B., Sremac, J., Aljinovič, D., Novak, M. & Skaberne, D. 2009: Late Variscan (Carboniferous to Permian) environments in the Circum Pannonian Region. -Geologica Carpathica, 60, 71–104.

Webster, R., 2000. Is soil variation random? Geoderma 97, 149–163.

Wennberg, O.P., Rennan, L. & Basquet, R. 2009: Computed tomography scan imaging of natural open fractures in a porous rock; geometry and fluid flow. -Geophysical Prospecting, 57 /2, 239–249. doi: 10.1111/j.1365-2478.2009.00784.x

Wesolowski, J.R. & Lev, H.M., 2005. CT: History, technology, and clinical aspects. Seminars in Ultrasound, CT and MRI 26, 376–379.

Withers P.J., Bouman C., Carmignato S., Cnudde V., Grimaldi D., Hagen C.K., Eric Maire E., Manley M., Plessis A. & Stock S., 2021: X-ray Computed Tomography. Nature Reviews Methods Primers, 1 ,18, 1 – 21. doi:10.1038/s43586-021-00015-4.

Withjack, E.M. 1988: Computed tomography for rock property determination and fluid flow visualization. - SPE Formation Evaluation, 3/4, 696-704. doi: 10.2118/16951-PA

Yang Y., Li Y., Yao J., Zhang K., Iglauer K., Luquot L. & Wang Z., 2019: Formation damage evaluation of a sandstone reservoir via pore-scale X-ray computed tomography analysis. Journal of Petroleum Science and Engineering, 183, 106356. doi.org/10.1016/j.petrol.2019.106356.

Yang, Y., Ayral, S. & Gryte, C.C. 1984: Computer-Assisted Tomography for the Observation of Oil Displacement in Porous Media. -Soc. Pet. Eng. J., 24/1, 53-55. doi: 10.2118/11758-PA.

Zhou Z., Gunter,W. & Jonasson R., 1995: Controlling formation damage using clay stabilizers: a review. In: Annual Technical Meeting. Petroleum Society of Canada, PETSOC, 95 – 71. doi: 10.2118/95-71.